UPPSALA
UNIVERSITET

Transition Metal-Based Electrocatalysts for Alkaline Water Splitting and CO$_2$ Reduction

ZHEN QIU

Dissertation presented at Uppsala University to be publicly examined in Polhemsalen, 10134, Ångström Laboratory, Lägerhyddsv. 1, Uppsala, Tuesday, 21 May 2019 at 13:15 for the degree of Doctor of Philosophy. The examination will be conducted in English. Faculty examiner: Professor Kevin Sivula (École polytechnique fédérale de Lausanne (EPFL)).

Abstract

Qiu, Z. 2019. Transition Metal-Based Electrocatalysts for Alkaline Water Splitting and CO_2 Reduction. *Digital Comprehensive Summaries of Uppsala Dissertations from the Faculty of Science and Technology* 1791. 87 pp. Uppsala: Acta Universitatis Upsaliensis. ISBN 978-91-513-0620-9.

With excessive usage of fossil fuels and ever-increasing environmental issues, numerous efforts have been devoted to the development of renewable energies for the replacement of traditional fossil fuels to reduce greenhouse gas emission and realize the rapidly growing demand for global energy. Renewable energies, however, often show diurnal and seasonal variations in power output, forming a need for energy storage to meet people's continuous energy supply. One approach is to use electrolysis and produce a fuel that can be used on demand at a later stage. A full realization of effective electricity-to-fuel conversion, however, is still limited by the large overpotential requirements as well as concerns with the usage of scarce platinum group elements. This thesis presents studies on transition metal-based electrocatalysts for alkaline water splitting and CO_2 reduction, which are two technologies to produce a chemical fuel from renewable electricity. Our aim is to develop efficient, inexpensive, and robust electrocatalysts based on earth-abundant elements with high energy conversion efficiencies.

In the first part, we develop and investigate three different electrocatalysts intended for high-performance electrocatalysis of water; NiO nanoflakes (NFs) with tuneable surface morphologies, Fe doped NiO nanosheets (NSs), and self-optimized NiFe layered double hydroxide (LDH) NSs. The self-assembled NiO NFs show drastically different performance for the oxygen evolution reaction (OER). Besides the morphology effect on the catalytic property, the presence of Fe is also functional to improve the catalytic activity for both OER and hydrogen evolution reaction (HER). The NiFe LDH NSs form the most effective system for the overall catalytic performance and is dramatically improved *via* a dynamic self-optimization, especially for HER, where the overpotential decreases from 206 mV to 59 mV at 10 mA cm^{-2}. In order to get insight into the interfacial reaction processes, a variety of techniques were performed to explore the underlying reasons for the catalytic improvement. *Ex-situ* X-ray photoelectron spectroscopy, transmission electron microscope and *in-situ* Raman spectroscopy were utilized to characterize and understand the oxidations states, the crystallinity and the active phases. Electrochemical impedance spectroscopy was applied to investigate the dominating reaction mechanisms during high-performance and stable electrocatalysis.

In the second part, dynamically formed $CuInO_2$ nanoparticles were demonstrated to be high-performance electrocatalysts for CO_2 reduction. *In-situ* Raman spectroscopy was utilized to reveal and understand the formation of $CuInO_2$ nanoparticles based on the Cu_2O pre-catalyst onto an interlayer of indium tin oxide under the electrochemical reaction. Density function theory calculation and *ex-situ* X-ray diffraction further prove the formation of $CuInO_2$ nanoparticles during vigorous catalysis. The findings give important clues on how Cu-based electrocatalysts can be formed into more active materials and can provide inspiration for other Cu-based intermetallic oxides for high-efficiency CO_2 reduction.

Keywords: Alkaline water splitting, CO2 reduction, Electrocatalyst, In-situ Raman spectroscopy.

Zhen Qiu, Department of Engineering Sciences, Solid State Physics, Box 534, Uppsala University, SE-751 21 Uppsala, Sweden.

A promise tomorrow is worth a lot less than trying today.

Dedicated to my family and friends
谨献给我的家人，挚友和青春！

List of Papers

This thesis is based on the following papers, which are referred to in the text by their Roman numerals.

I.   **Zhen Qiu,** Yue Ma, Kristina Edström, Gunnar A. Niklasson, Tomas Edvinsson. (2017) Controlled crystal growth orientation and surface charge effects in self-assembled nickel oxide nanoflakes and their activity for the oxygen evolution reaction. *International Journal of Hydrogen Energy*, 42(47):28397-28407

II. **Zhen Qiu**, Yue Ma, Tomas Edvinsson. *In operando* Raman spectroscopy of surface phase transformation in iron-doped nickel oxide nanosheets for enhanced overall water splitting. *Submitted to Nano Energy*.

III. **Zhen Qiu**, Yue Ma, Gunnar A. Niklasson, Tomas Edvinsson. An electrochemical impedance study of alkaline water splitting using nickel (iron) oxides nanosheets. *In manuscript.*

IV. **Zhen Qiu**, Cheuk-Wai Tai, Gunnar A. Niklasson, Tomas Edvinsson. (2019) Direct observation of active catalyst surface phases and the effect of dynamic self-optimization in NiFe-layered double hydroxides for alkaline water splitting. *Energy & Environmental Science*, 12:572-581.

V.   Roghayeh Imani, **Zhen Qiu**, Reza Younesi, Meysam Pazoki, Daniel L. A. Fernandes, Pavlin D. Mitev, Tomas Edvinsson, Haining Tian. (2018) Unravelling in-situ formation of highly active mixed metal oxide $CuInO_2$ nanoparticles during CO_2 electroreduction. *Nano Energy*, 49:40-50.

Paper IV is published with open access. Other reprints were made with permission from the respective publishers.

My contribution

I.   A major part of experiments, characterizations, data analysis, and manuscript writing.

II.   A major part of experiments, characterizations, data analysis, and manuscript writing.

III. A major part of experiments, characterizations, data analysis, and manuscript writing.

IV.   A major part of experiments, characterizations, data analysis, and manuscript writing.

V.   Main contribution on *in-situ* Raman measurements, SEM images with EDS results, and part of the analysis and manuscript writing.

Papers not included in the thesis

VI. İlknur Bayrak Pehlivan, Miguel A. Coyotzi, **Zhen Qiu**, Gunnar A. Niklasson, Tomas Edvinsson. (2019) Impedance spectroscopy modeling of nickel-molybdenum alloys on porous and flat substrates for applications in water splitting. *Submitted* to *The Journal of Physical Chemistry C*.

VII. Yuanyuan Han,* **Zhen Qiu**,* Ganesh N. Oommen P. Varghese, Jöns Hilborn, Bo Tian, Klaus Leifer. (2019) MicroRNA detection based on duplex-specific nuclease-assisted target recycling and gold nanoparticle/graphene oxide nanocomposite-mediated electro-catalytic amplification. *Biosensors & Bioelectronics*, 127:188-193.

VIII. Miguel A. Arvizu, Hui-Ying Qu, Umut Cindemir, **Zhen Qiu**, Edgar A. Rojas-González, Daniel Primetzhofer, Claes G. Granqvist, Lars Österlund, Gunnar A. Niklasson. (2019) Electrochromic WO_3 thin films attain unprecedented durability by potentiostatic pretreatment. *Journal of Materials Chemistry A*, 7:2908-2918.

IX. Chenjuan Liu, **Zhen Qiu**, Willian R. Brant, Reza Younesi, Yue Ma, Kristina Edström, Torbjörn Gustafsson, Jiefang Zhu. (2018) A free standing Ru-TiC nanowire array/carbon textile cathode with enhanced stability for $Li-O_2$ batteries, *Journal of Materials Chemistry A*, 6(46):23659-23668.

X. Hui-Ying Qu, Daniel Primetzhofer, **Zhen Qiu**, Lars Österlund, Claes G. Granqvist, Gunnar A. Niklasson. (2018) Cation/anion□ based electrochemical degradation and rejuvenation of electro-chromic nickel oxide thin films. *ChemElectroChem.*, 5(22):3548-3556.

XI. Bo Tian, **Zhen Qiu**, Jing Ma, Marco Donolato, Mikkel Fougt Hansen, Peter Svedlindh, and Mattias Strömberg. (2018) On-Particle rolling circle amplification based core-satellite magnetic super-structures for microRNA detection. *ACS applied materials & interfaces*, 10(3):2957-2964.

XII. Gunnar A. Niklasson, **Zhen Qiu**, İlknur Bayrak Pehlivan, and Tomas Edvinsson. (2018). Impedance Spectroscopy of Water Splitting

Reactions on Nanostructured Metal-based Catalysts. *In 12th International Scientific Conference on Functional Materials and nanotechnologies, Riga, Latvia,* Oct 2-5, 2018. (p. 100).

XIII.   Sagar M. Jain, Dibya Phuyal, Matthew L. Davies, Meng Li, Bertrand Philipp, Catherine De Castro, **Zhen Qiu**, Jinhyun Kim, Trystan Watson, Wing Chung Tsoi, Olof Karis, Håkan Rensmo, Gerrit Boschloo, Tomas Edvinsson, James R. Durrant. (2018) An effective approach of vapour assisted morphological tailoring for reducing metal defect sites in lead-free, $(CH_3NH_3)_3Bi_2I_9$ bismuth-based perovskite solar cells for improved performance and long-term stability. *Nano Energy*, 49, 614-624.

XIV.   Bo Tian, Erik Wetterskog, **Zhen Qiu**, Teresa Zardán Gómez de la Torrea, Marco Donolato, Mikkel Fougt Hansen, Peter Svedlindh, Mattias Strömberg. (2017) Shape anisotropy enhanced optomagnetic measurement for prostate-specific antigen detection via magnetic chain formation. *Biosensors and Bioelectronics*, 98:285-291.

XV.   Bo Tian, Jing Ma, **Zhen Qiu**, Teresa Zardán Gómez de la Torre, Marco Donolato, Mikkel Fougt Hansen, Peter Svedlindh, and Matttias Strömberg. (2017) Optomagnetic detection of microRNA based on duplex-specific nuclease-assisted target recycling and multilayer core-satellite magnetic superstructures. *ACS nano*, 11(2):1798-1806.

XVI.   Hui-Ying Qu, Daniel Primetzhofer, Miguel A. Arvizu, **Zhen Qiu**, Umut Cindemir, Claes G. Granqvist, Gunnar A. Niklasson. (2017) Electrochemical rejuvenation of anodically coloring electrochromic nickel oxide thin films, *ACS Applied Materials & Interfaces*, 9(49), 42420-42424.

XVII.   Sagar Motilal Jain, **Zhen Qiu**, Leif Häggman, Mohammad Mirmohades, Malin B. Johansson, Tomas Edvinsson, Gerrit Boschloo. (2016) Frustrated Lewis pair-mediated recrystallization of $CH_3NH_3PbI_3$ for improved optoelectronic quality and high voltage planar perovskite solar cells. *Energy & Environmental Science*, 9(12), 3770-3782.

XVIII.   Bo Tian, **Zhen Qiu**, Jing Ma, Teresa Zardán Gómez de la Torre, Christer Johansson, Peter Svedlindh, Mattias Strömberg. (2016). Attomolar zika virus oligonucleotide detection based on loop-mediated isothermal amplification and AC susceptometry. *Biosensors & Bioelectronics*, 86, 420-425.

*Authors contributed equally to this work.

Contents

Abbreviations

AC	Alternating current
BF	Bright-field
C	Capacitance
CBD	Chemical bath deposition
C_{dl}	Double-layer capacitance
CPE	Constant phase element
CV	Cyclic voltammetry
DC	Direct current
DF	Dark-field
DFT	Density functional theory
DI	Deionized
EC	Equivalent circuit
ECSA	Electrochemical active surface area
EDS	Energy dispersive X-ray spectroscopy
EELS	Electron energy loss spectroscopy
EIS	Electrochemical impedance spectroscopy
Eqn.	Equation
F	Faraday constant
FTO	Fluorine-doped tin oxide
GC	Glassy carbon
G^o	Molar standard Gibbs free energy
HER	Hydrogen evolution reaction
H-NiFe LDH	NiFe LDH after 100 h HER reaction
HR-TEM	High-resolution transmission electron microscopy
ITO	Indium tin oxide
J	Current density
J_0	Exchange current densities
L	Inductance
LDH	Layered double hydroxide
LSV	Linear sweep voltammetry
M	Active sites
NFs	Nanoflakes
NHE	Normal hydrogen electrode
NS	Nanosheets
OER	Oxygen evolution reaction
O-NiFe LDH	NiFe LDH after 100 h OER reaction

PEM	Polymer electrolyte membrane
PVA	Poly(vinyl alcohol)
PZC	Point of zero charge
R_{ct}	Charge/electron transfer resistance
RHE	Reversible hydrogen electrode
SAED	Selected area electron diffraction
SCCM	Standard cubic centimeter per minute
SEM	Scanning electron microscopy
SHE	Standard hydrogen electrode
SOE	Solid oxide electrolyte
STEM	Scanning transmission electron microscopy
STH	Solar to hydrogen
T	Kelvin temperature
TEM	Transmission electron microscopy
XPS	X-ray photoelectron spectroscopy
XRD	X-ray diffraction
Y	Admittance
Z'	Real part of impedance
Z''	Imaginary part of impedance
Z_0	Magnitude of impedance
V	Voltage

c	Velocity of light
f	Frequency of alternating current voltage
h	Planck constant
η	Overpotential
λ	Wavelength
μ	Dipole
σ	Wavenumber
τ	Mean size of the crystallite size
υ	Frequency of light
φ	Phase angle

1. Introduction

1.1 Needs for renewable energy and storage

In modern society, our lives are crucially dependent on energy and currently, the dominating global energy is mainly supplied by traditional fossil fuels, *e.g.,* oil, natural gas, and coal. Figure 1.1 illustrates the world total primary energy supply by fuels in 2016, with 81.1% of net-emission fossil fuels including 27.1% of coal, 31.9% of oil, and 22.1% of natural gas, respectively. Forecasts predict growth by more than 25% to 2040 (International Energy Agency, 2018). However, fossil fuels are non-renewable and provide a net-emission of carbon dioxide (CO_2) into the atmosphere, which already results in visible changes of the world's climate (Dresselhaus and Thomas, 2001; Hoegh-Guldberg et al., 2018). Owing to the excessive use of fossil fuels, ever-increasing environmental issues, and a globally growing population, there is a high demand for renewable alternatives and clean energy sources (Liu et al., 2010; Seh et al., 2017).
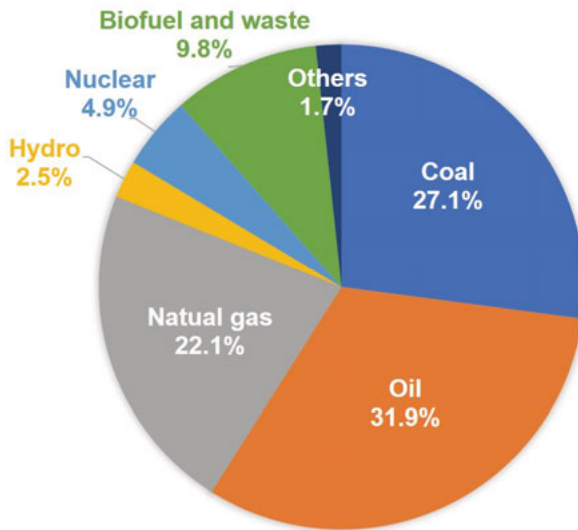

Figure 1.1 The world total primary energy supply by fuels in 2016. © The data is collected from IEA (International Energy Agency) 2019 Key Energy Statics, IEA publishing.

Sunlight, wind and tidal energies are regarded as preeminent environmentally friendly renewable energy sources, and their ability to meet people's future energy needs has been well documented (Barber, 2009; Lewis and Nocera, 2006; Nocera, 2006). One of the challenges confronting their large-scale usage is their intermittent nature, and thus a need to equilibrate their output or store the energy for later use (Larcher and Tarascon, 2015). Given the intermittent changes by the atmospheric conditions, the development of efficient storage technologies is important to enable the growth of renewable electricity towards a situation where they can be the primary energy supply. One prospective approach is to develop electrochemical technologies enabling efficient conversion of molecules in Earth's atmosphere (*e.g.*, H_2O, CO_2, and N_2) into chemical fuels (*e.g.*, hydrogen, hydrocarbons, and ammonia) *via* the integration of such systems with renewable electricity (Seh et al., 2017). Figure 1.2 illustrates the available catalytic conversion pathways for renewable fuels. The universal feedstock (*e.g.*, H_2O, CO_2, and N_2) can be potentially converted into the aforementioned products by electrochemical processes coupled to renewable energies (*e.g.,* solar, wind). Conversion of intermittent energies into chemical fuels with a zero net-emission would enable a sustainable supply of energy without any net change in the atmospheric conditions. This thesis is devoted to developing and understanding of earth-abundant electrocatalysts with the required characteristics to split water into H_2 and O_2 as well as perform CO_2 reduction with high conversion efficiency.
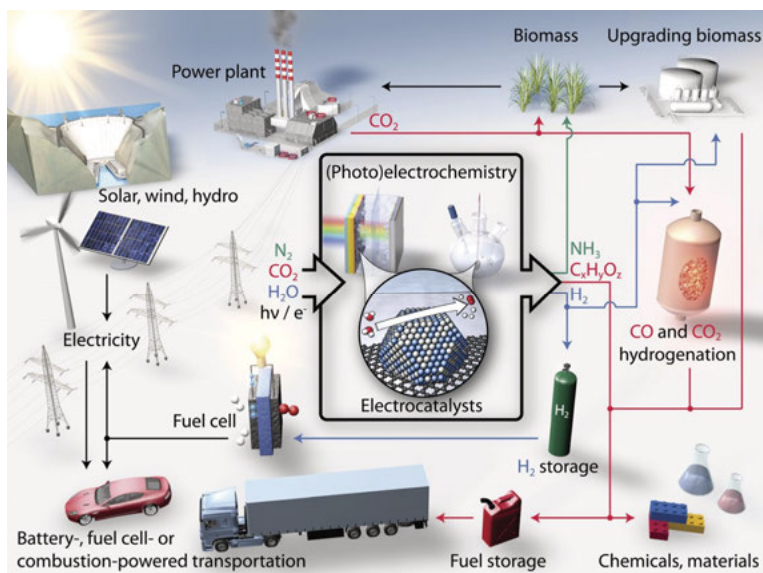

Figure 1.2 Schematic of available energy conversions based on electrocatalysis. ©
Reprinted with permission from (Seh et al., 2017)

1.2 Hydrogen energy

Molecular hydrogen contains the highest energy density per mass (0.0899 kg/Nm^3) of any chemical compound in the universe and is also a carbon-neutral chemical and would as such be an ideal energy carrier to power to sustainable civilization. It is versatile to be used for heat (Dodds and Demoullin, 2013), industry refining processes (Napp et al., 2014), and for providing electricity in stationary (Ball and Weeda, 2015) and transport/vehicle applications *via* fuel cells (Crabtree et al., 2004; Tollefson, 2010) Presently, up to 96% of the hydrogen used in the world is derived from steam reforming of natural gas, and only about 4% of the hydrogen is produced from water decomposition (Balat, 2008; Pilavachi et al., 2009). Even though steam reforming is the cheapest way to produce hydrogen today, the large quantities of CO_2 emission prevent a large increase in this production technology (Turner, 1999; Whiteley et al., 2000). As discussed in Chapter 1.1, hydrogen can also be produced by renewable electricity. Figure 1.3 shows the possible pathways to generate hydrogen by solar energy which contains thermolysis, biomass, photolysis, and electrolysis. Thermolysis can split water directly at high temperatures, sadly suffering from the recombination of hydrogen and oxygen at that high temperature, inhibiting its forward efficiency. Biomass conversion for hydrogen production is inefficient and expensive, which cannot meet the global economy and energy demands without substantially decrease the land necessary for cultivation of food. The low conversion efficiency and instability of photolysis limit its practical application (Osterloh, 2013). The realization of large-scale hydrogen production coupled to renewable energies is instead largely dependent on the cost-efficiency catalysts and the development of green technologies (Crabtree et al., 2004). Water electrolysis coupled to sources of renewable electricity is regarded as the simplest approach and anticipated to form a major contribution to future hydrogen production (Turner, 1999; Whiteley et al., 2000). Compared with other available technologies, water electrolysis has the absolute advantage to produce extremely pure hydrogen (>99.9%), ideal also for special demands in industry, for example, the manufacture of some electronic components that require the addition of high purity hydrogen (Pletcher and Li, 2011). Very recently, an economic analysis of production of hydrogen from renewable electricity based on the market situations in Texas, USA and Germany, showed a production price of $3.23 kg^{-1} (Glenk and Reichelstein, 2019) cheap enough for niche applications such as in fuel cell vehicles but not yet competitive with industrial-scale supplies from steam reforming of natural gas ($2.67 per kilogram) (Tollefson, 2010).
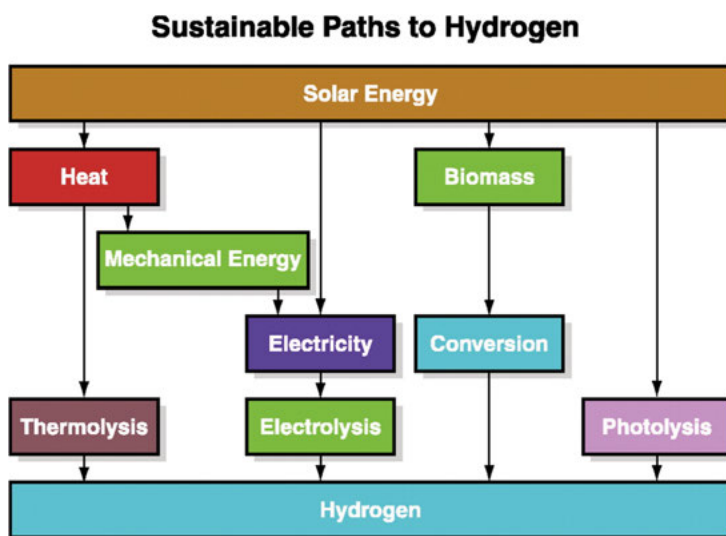
Sustainable Paths to Hydrogen

Figure 1.3 Sustainable pathways for hydrogen generation from solar energy. © Reprinted with permission from (Turner, 1999)

1.3 Water electrolysis

1.3.1 Historical background

Electrolysis of water was shown already in 1789 by Deiman and van Troostwijk using a Leyden jar (van Troostwijk and Deiman, 1789) and subsequently in 1800 by Nicholson and Carlisle in their experiments on the electrolytic splitting of water using photovoltaic piles. Following the electrification of society, over 400 industrial water electrolyzers were in use in 1902 (Kreuter and Hofmann, 1998), while the strong interest in light-driven electrolysis did not start until the seminal paper by Fujishima and Honda in 1972 (Fujishima and Honda, 1972), using TiO_2 as a photoanode and platinum as a cathode with a slight voltage bias from the different electrolyte concentrations in the separated cells. The water electrolysis technology developed rapidly between the 1920s and the 1970s. In the first half of the 20th century, with the huge demand for hydrogen to produce ammonia fertilizer, water electrolysis technology was largely stimulated by the low cost of hydropower at that time. However, when hydrocarbon energy began to be applied in the industry on a large scale, hydrogen produced by steam reforming of natural gas and coal quickly took over the market. At that time, the progression and further development of hydrogen generation by water electrolysis decreased. Until the oil crisis of the 1970s, interest in water electrolysis to hydrogen production was meager but has since been revived (White et al., 1984). Currently, due to the need of

decreasing our usage of fossil fuels, a revitalized interest is seen where improving the catalytic efficiency of water splitting reaction in a sustainable and cheap way is one of the major challenges.

1.3.2 Types of water electrolysis

Figure 1.4 shows a schematic illustration of a water electrolysis setup composed of an anode, a cathode, an external power supply, and a conductive electrolyte. Under the applied voltage, hydrogen and oxygen are produced on the cathode and anode, respectively. At room temperature and using neutral water, the electrolysis of water proceeds slowly because pure water does not have a good electric conductivity with only 10^{-7} M of ion concentration. Therefore, in general, acid, alkaline or salts are added to improve the conductivity of the electrolyte. In addition, different geometries and solutions are used to ensure that the redox reactions occur close to each other but still keep the recombination low. According to different types of electrolytes used and approaches to separate the reactions, water electrolysis can be divided into three main classifications; alkaline water electrolysis, polymer electrolyte membrane (PEM) water electrolysis, and solid oxide electrolyte (SOE) water electrolysis. Their respective main charge carriers and temperature characteristics are presented in Table 1.1.
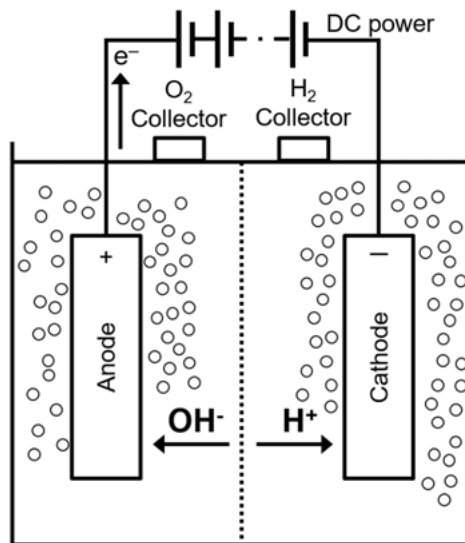

Figure 1.4 Schematic illustration of a water electrolysis cell where oxidation of oxygen in water occurs at the anode and reduction of hydrogen occurs at the cathode.

Table 1.1 Types and Characteristics of Water Electrolysis. This table is adapted from *(Rashid et al., 2015)*

Electrolysis technology	Alkaline water electrolysis	Polymer electrolyte membrane (PEM) electrolysis	Solid oxide electrolyte (SOE) electrolysis
Anode reaction OER	$2OH^-\rightarrow 2e^-+H_2O+\frac{1}{2}O_2$	$H_2O\rightarrow 2e^-+\frac{1}{2}O_2+2H^+$	$O^{2-}\rightarrow 2e^-+\frac{1}{2}O_2$
Cathode reaction HER	$2e^-+2H_2O\rightarrow 2OH^-+H_2$	$2e^-+2H^+\rightarrow H_2$	$2e^-+H_2O\rightarrow O^{2-}+H_2$
Charge carrier	OH^-	H^+	O^{2-}
Operating temperature range	40–$90\ ^{o}C$	20–$100\ ^{o}C$	700–$1000\ ^{o}C$

PEM electrolyzers are considered to be the most promising technology for producing high-purity hydrogen coupled to renewable energies, *e.g.*, solar, wind, and hydroelectric power (Barbir, 2005) because it has high efficiencies operating at a moderate temperature, and can be effective also with a variable input. The strong acidic environment in PEM electrolyzers, however, vastly limits the range of materials that can be used at the electrodes (Reier et al., 2017). A good conducting material with a suitable work function that does not corrode implies noble metals, at least at the cathode side. One concern is that the noble electrocatalysts are quite costly and not earth-abundant enough for large scale global implementation. SOE electrolyzer consumes less energy than conventional low-temperature water electrolyzer, because of the improved reaction thermodynamic and kinetic working at high temperatures. Unfortunately, high temperatures are also connected with severe corrosion issues (Santos et al., 2013). Alkaline water electrolysis, on the other hand, is a quite mature process and have been used for commercial hydrogen production for a long time (Holladay et al., 2009; Zeng and Zhang, 2010), where the electrolytes normally are highly concentrated KOH or NaOH in aqueous solution. Alkaline water electrolysis is considered as a possible future route for coupling to renewable electricity because of its good stability and simplicity (Holladay et al., 2009; Zeng and Zhang, 2010). It has recently also been suggested to be more efficient than the PEM approach if thinner separators than the conventional ones are used (Schalenbach et al., 2016). Noble metals and their compounds are generally considered to be too rare to be supplied for the practical hydrogen production at a large scale. Nickel (Ni), Iron (Fe), Cobalt (Co), Molybdenum (Mo), their alloys and oxides are instead regarded as the main base family of electroactive catalysts with good corrosion resistance in an alkaline solution after the formation of a passivating layer and are the dominating electrocatalysts used in industrial applications and almost as popular in research for the development of alkaline water electrolysis.

1.4 Alkaline water splitting

1.4.1 Thermodynamics

Electrochemical water splitting can be described by two half-reactions: the water oxidation half-reaction at the anode (oxygen evolution reaction, OER) and water reduction half-reaction at the cathode (hydrogen evolution reaction, HER). Theoretically, the minimum required potential to split water into hydrogen and oxygen is the thermodynamic reversible potential of the reaction, which is related to the change in Gibbs free energies of the involved reactants and products. At the regular atmospheric pressure (0.101 MPa), the minimum voltage can be calculated as Eqn. 1.1

$$E_{rev,\,t}^{o} = \frac{1}{2F}(G_{H_2}^{o} + 0.5G_{O_2}^{o} - G_{H_2O(l)}^{o})_t \qquad (1.1)$$

where G^o is the molar standard Gibbs free energy, F is the Faraday constant, t is the reaction temperature in Celsius, in Kelvin scale $T = 273.15\ K + t$. In the temperature range of 25–200 °C, E_{rev}^{o} can be expressed as Eqn. 1.2 (LeRoy, 1983).

$$E_{rev,\,t}^{o} = 1.584 - 1.5421 \times 10^{-3}T + 9.523 \times 10^{-5}T\,lnT + 9.84 \times 10^{-8}T^2 \qquad (1.2)$$

At the temperature of 298.15 K and 1 atm, the minimum thermodynamic reversible potential is 1.229 V, which is equal to a minimum Gibbs energy of 237.18 kJ mol^{-1}. The operating principle of the overall alkaline water splitting is illustrated in Figure 1.5a. The respective half-reaction that occurs at the anode and the cathode in 1 M alkaline electrolyte can be expressed as follows, where RHE is the reversible hydrogen electrode potential.
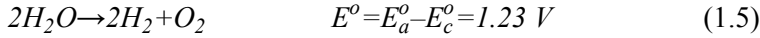
Cathode reaction (HER)

$$4e^- + 4H_2O \rightarrow 4OH^- + 2H_2 \qquad\qquad E_c^o = 0\ V\ vs\ RHE \qquad (1.3)$$

Anode reaction (OER)

$$4OH^- \rightarrow 4e^- + 2H_2O + O_2 \qquad\qquad E_a^o = 1.23\ V\ vs\ RHE \qquad (1.4)$$

Overall reaction

$$2H_2O \rightarrow 2H_2 + O_2 \qquad\qquad E^o = E_a^o - E_c^o = 1.23\ V \qquad (1.5)$$

To drive this uphill reaction in practice, additional energy is required due to the sluggish reaction kinetics of catalysts as shown in Figure 1.5b. The total voltage required for water splitting can be formulated as Eqn. 1.6.

$$E_{total} = 1.23\ V + \eta_a + |\eta_c| + iR \qquad (1.6)$$

where 1.23 V is the thermodynamic reversible potential at 298.15 K and 1 atm, η_a and η_c denote the anodic and cathodic overpotentials at a certain current density, and iR is the voltage drop in the electrochemical setup, determined by Ohm's law.
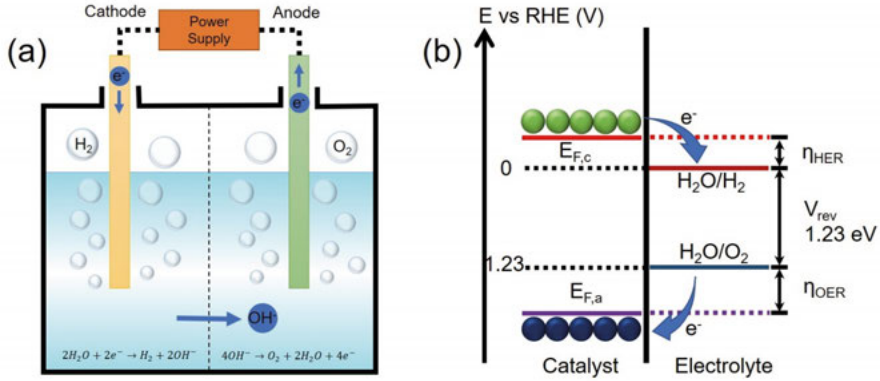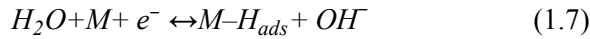
Figure 1.5 Schematic illustration of (a) the operating principle of the overall alkaline water splitting in electrolysis, (b) the energy levels involved in water splitting with the overpotentials of the HER and OER indicated.
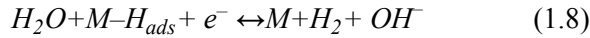
1.4.2 Reaction mechanism

Hydrogen evolution reaction

The mechanism of the HER in alkaline solution is typically considered to be a combination of three primary steps: Volmer step (Eqn. 1.7), defined by the water discharge which involves dissociation into OH⁻ and formation of adsorbed hydrogen; followed by either Heyrovsky step (Eqn. 1.8), an electrochemical desorption process or Tafel step (Eqn. 1.9), a chemical desorption process, where M denotes active sites on the electrode, H_{ads} represents a free hydrogen atom adsorbed on the electrode (Nørskov et al., 2005; Stamenkovic et al., 2017).

Volmer step

$$H_2O + M + e^- \leftrightarrow M–H_{ads} + OH^- \qquad (1.7)$$

Heyrovsky step

$$H_2O + M–H_{ads} + e^- \leftrightarrow M + H_2 + OH^- \qquad (1.8)$$

Tafel step

$$2M–H_{ads} \leftrightarrow 2M + H_2 \qquad (1.9)$$

The catalytic reaction rate is greatly determined by the strength of the H_{ads}–M interaction, which can be estimated by the free energy of hydrogen adsorption ΔG_{Hads} (Cook et al., 2010; Parsons, 1958; Seh et al., 2017). Figure 1.6

shows an experimental plot of the logarithm of the exchange current densities (J_0) against the energy of chemisorption of hydrogen on different metals (H_{ads}–M) for HER in acidic solution, which was performed by Trasatti (Trasatti, 1972). The right slope of the experimental volcano plot corresponds to the metals with large and negative ΔG_{Hads}. In this situation, H_{ads} interacts strongly with the surface, which leads to a fast discharge step but remarkably restricts subsequent protonation or recombination steps. The left slope corresponds to metals with large and positive ΔG_{Hads}. In this case, adsorbate forms a weak bond with the surface, resulting in a slow discharge step that limits the overall turnover rate. In short, if the strength is too weak, the adsorption (Volmer) step will retard the overall rate, whereas if the strength is too strong, the desorption (Heyrovsky/Tafel) step will limit the overall reaction rate. Hence, an appropriate condition for an active HER catalyst is ΔG_{Hads} near to zero, necessary but not insufficient. In other words, any element whose volcano position is close to zero will be expected to be an efficient HER catalyst, such as Pt.
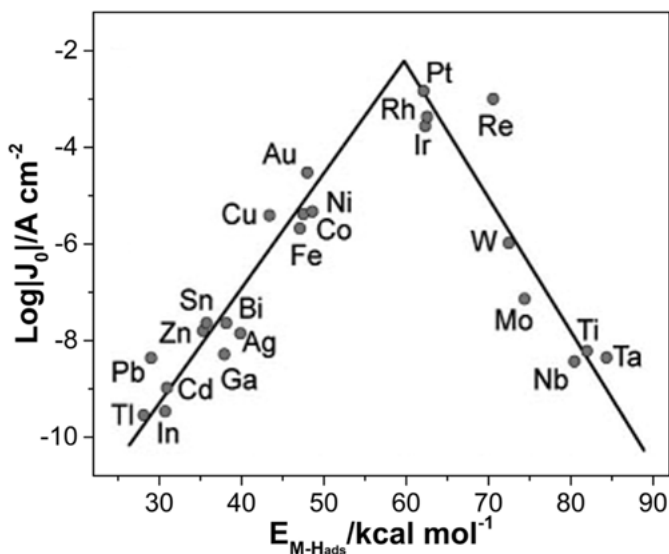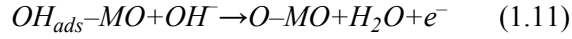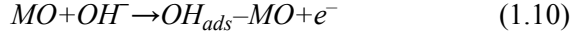

Figure 1.6 Volcano curve for HER on metal electrodes in acidic media. © Adapted with permission from (Cook et al., 2010). Copyright 2010 American Chemical Society.
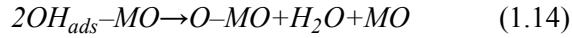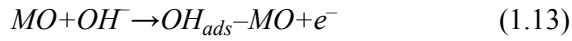
Oxygen evolution reaction

Compared with HER, OER requires a higher driving force to overcome the kinetic barrier because it is a four electron-proton coupled reaction (Suen et al., 2017), which means that it exists many kinds of possible activation steps determining the overall reaction rate. There are several possible reaction mechanisms of OER on oxides in alkaline solution as reported (Matsumoto and Sato, 1986; Xiao et al., 2015), however, here we will mainly consider the

two most recognized pathways: the electrochemical oxide path (Eqn. 1.10-1.12) and the oxide path (Eqn. 1.13-1.15).

Electrochemical oxide path:

$$MO+OH^- \rightarrow OH_{ads}-MO+e^- \tag{1.10}$$

$$OH_{ads}-MO+OH^- \rightarrow O-MO+H_2O+e^- \tag{1.11}$$

$$2O-MO \rightarrow 2MO+O_2 \tag{1.12}$$

Oxide path:

$$MO+OH^- \rightarrow OH_{ads}-MO+e^- \tag{1.13}$$

$$2OH_{ads}-MO \rightarrow O-MO+H_2O+MO \tag{1.14}$$

$$2O-MO \rightarrow 2MO+O_2 \tag{1.15}$$

M denotes the active sites on the electrode, and OH_{ads} denotes a hydroxyl atom adsorbed on the surface.

As mentioned above, there are different kinds of activation steps determining the rate of OER activity. In these two pathway cases, the approach to form the O–MO intermediates is different. One is through the combination of OH_{ads}–MO with OH^- to form O–MO, whereas the other one is to combine 2O–MO directly to produce the O–MO intermediates. There are at least two main factors to determine the catalytic activity of materials for OER. One is the bond strength of M–O in the intermediate states, which is similar to the HER principle. Another is the rate of electron transfer occurs that at the intersection as shown in Figure 1.7, in keeping with the Franck-Condon principle (Matsumoto and Sato, 1986). In this case, the Fermi level and the overlapping degree between electronic states of the electrode related to the exposed areas and the adsorbed species play a crucial role in the reaction rate. Hence, it is of importance to figure out the adsorbed species at each thermal equilibrium.
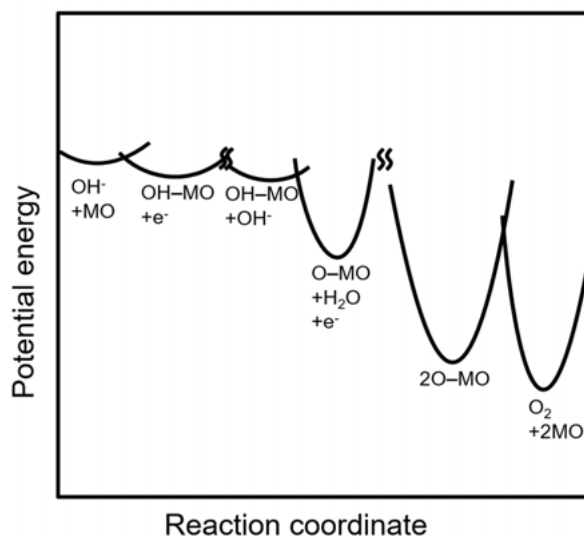
Figure 1.7 Potential energy diagrams for a rate-determining oxygen desorption mechanism in the electrochemical oxide path in the alkaline solution shown in Eqn. 1.13-1.15. © Adapted with permission from (Matsumoto and Sato, 1986)

1.4.3 Key parameters evaluated for electrocatalytic activity

In recent years, continuous efforts have been devoted to the development of efficient, durable and inexpensive catalysts for electrochemical water splitting. The major goal is to reduce the energy barrier and thereby improve electrocatalytic efficiency. Usually, the catalytic performance of gas evolution is mainly evaluated by measuring the catalytic current density or the amount of gas generated. The two half-reactions of water splitting are both in strongly polarized conditions. Although hydrogen and oxygen evolution proceed at the cathode and anode respectively, key experimental parameters are the same to evaluate their overall electrocatalytic activity, where the main ones in electrocatalysis are:

Current density (J)

Table 1.2 clarifies advantages and drawbacks of four widely used current normalization methods, which has been thoroughly discussed by Anantharaj, S et al. (Anantharaj et al., 2016). Any of these current normalization methods are accepted by the research community, but in order to compare fairly with earlier reports, and previously published results it is better to use geometrical surface area normalized current density.

24

Table 1.2 Comparison of Various Current Normalization Methods for Electrocatalytic Water Splitting.

This table is adapted from (Anantharaj et al., 2016)

Normalization method	Merits	Demerits
Geometrical surface area	Widely accepted and used the method. A fair comparison with published reports. It is easy. Good for planar electrodes such as foils and deposited thin films.	Does not reflect the intrinsic catalytic property of the material. May vary depending on catalyst loading and its optimization. Geometrical area of the substrate electrode is not equal to the actual surface area of the catalyst participating in catalysis.
Electro-chemical Surface Area (ECSA)	Can reflect the intrinsic catalytic property of the catalyst. Loading-sensitive.	Difficulties in determining the ECSA. Large experimental inaccuracies between one method and other, such as CV and EIS studies comparison with existing reports would be tedious.
Brunauer–Emmett–Teller (BET) surface area	Ease of determining the BET surface area. Most suitable for porous materials and catalysts. Loading-sensitive.	Does not reflect the intrinsic catalytic property of the catalyst. Leads to large errors because not all gas adsorption sites are electrochemically active not suitable for planar and thin film electrodes.
Catalyst loading	Directly cares about the loading regardless of the type of catalyst. Suitable to compare when the same material is used at different loadings.	Direct comparison with theory and experiment is not feasible. Does not reflect the intrinsic catalytic property of the material. Comparison of catalysts of varying particle size (*e.g.*, mono- and polydispersed catalysts), density (*e.g.*, metals and metal aerogels), morphology (*e.g.*, catalysts with spherical, rod, wire, and sheet structures), and topography (*e.g.*, catalysts with smooth and rough surfaces) is not possible. Comparison with existing reports is also not possible.

Overpotential (η)

The overpotential (η) at a certain current density is one of the most important indicators when evaluating the performance of electrocatalysts. In an ideal case, the applied energy for reaction proceeding will be equal to the reaction potential at equilibrium. However, in a real system, the applied potential is usually larger than the equilibrium potential for a specific reaction because of the reaction energy barrier. The difference between the applied potential and equilibrium potential is defined as overpotential, which is given by Eqn. 1.16

$$\eta = E - E_{rev} \qquad\qquad (1.16)$$

In principle, the measured overpotential is mainly from three parts: the activation overpotential, the concentration overpotential, and the system overpotential owing to uncompensated resistance. The activation overpotential is largely dependent on the intrinsic property of each catalyst. The concentration overpotential occurs when there is a sudden concentration drop near the interface. It can be minimized by stirring the electrolyte or having a highly concentrated electrolyte. The resistance overpotential can be eliminated by ohmic drop compensation (iR-compensation), which can be done manually or by the system setting in the electrochemical work station.

When combined with solar energy to produce hydrogen, the overpotential at 10 mA cm^{-2} (geometrical surface area) is considered as a standard value to evaluate the indicated catalytic efficiency (McCrory et al., 2013, McCrory et al., 2015), because the current density of 10 mA cm^{-2} is roughly in the range of most PV systems delivering voltage enough to split water, and corresponds to 12.3% of solar to hydrogen efficiency under one sun illumination if assuming there is no loss of Faradic efficiency of catalysts.

Stability

The stability is another essential parameter to evaluate materials' potential for the practical application. Usually, it can be estimated by cyclic voltammetry (CV) cycling with a high scan rate, which is considered as an accelerate degradation analysis and chronopotentiometric or chronoamperometric test operating at a constant potential or current. Now, it has been widely adopted that an invisible change of current density for more than 12 h by chronoamperometric test or insignificant increase in overpotential at a selected current density (*e.g.,* 10 mA cm^{-2}) for more than 12 h by chronopotentiometry is enough to identify the high efficiency of catalysts. The variation in catalyst material thickness and actual current densities in-between studies incorporates further complexities. A short time measurement will not capture degradations of the catalyst material if it is too thick for these effects to be apparent, and measurements performed with a low current density will additionally show a naturally slow material decomposition.

Tafel Slope and exchange current density (J_0)

The electrochemical kinetics can approximately be described by the Butler-Volmer equation, which is expressed by Eqn. 1.17, where J_0 is the exchange current density, α is the transfer coefficient of the anode or the cathode ($\alpha_a + \alpha_c = 1$, usually, $\alpha_a = \alpha_c = 0.5$), F is faradays constant, T is absolute temperature, and n is the number of transferred electrons (OER involves four electrons while HER involves two electrons).

$$J = J_0[exp(\frac{\alpha_a nF\eta_a}{RT}) - exp(\frac{\alpha_c nF|\eta_c|}{RT})] \tag{1.17}$$

The Tafel plot of an electrocatalytic process is generally obtained by replotting a polarization curve as a plot of $log\ J\ vs$ overpotential η, which can be derived from Butler-Volmer equation assuming that the applied potential is far away from the equilibrium potential with large overpotential ($|\eta| \gg RT/nF$) denoted as Eqn. 1.18. The overpotential used here is without resistance overpotential by iR compensation.

$$\frac{d\ log|J|}{d\eta} = 2.303RT/\alpha nF \tag{1.18}$$

The Tafel plot is often used as a primary parameter to determine or compare the catalytic activity. In general, the catalysts that have a good charge transfer ability will be expected to show a small Tafel slope, signifying fast reaction kinetics when η is at the y-axis. But it is notable that the Tafel slope is only a quantitative characterization to reveal different electrocatalytic kinetics and mechanisms of electrocatalytic activity, because it depends on the assumptions that a series of factors are constant, such as the value of a symmetry factor, surface coverage, etc. (Anantharaj et al., 2016a; Bockris, 1956; Shi and Zhang, 2016)

The value of J_0 can be calculated by Eqn. (1.18) and visualized with the corresponding Tafel plot at zero overpotential and reflects the intrinsic bonding/charge transferring interactions between electrocatalyst and reactant. As high exchange current density (J_0) as possible is naturally desired for the electrocatalyst of the target reaction (Suen et al., 2017).

1.5 Electrocatalytic CO$_2$ reduction

As an important trace gas in Earth's atmosphere, CO_2 is an essential raw feedstock for photosynthesis. Nevertheless, the excessive use of non-renewable fossil fuel has caused increased emission of CO_2, inducing serious environmental and climate issues. Moreover, the global CO_2 emission is still growing, showing a 1.6% increase in 2017 and about 2.7% in 2018 reported in the Global Carbon Project (CO_2 Emissions Reached an All-Time High in 2018).

The excessive emission of CO_2 has caught intensive attention and driven increasing interest by investors and researchers (Nocera, 2017; Vasileff et al., 2017; Zhang et al., 2017). To achieve a stable ecological environment and keep a virtuous circle in a route towards a sustainable society, the CO_2 gas generated into the earth's atmosphere should be roughly the same amount as the consumed amount. By mimicking the photosynthesis process of green plants on an industrial level, one promising approach is to convert CO_2 emissions in a closed cycle from factories into other useful carbonaceous fuels and chemicals to be used again.

At present, there are several routes enabling convert CO_2 into useful molecular fuels or harmless minerals, including electrochemical (Graciani et al., 2014), Photoelectrochemical (Yu et al., 2014), indirect mineral sequestration (Ko et al., 2012) and biological (Mondal et al., 2016) methods. Among them, the electrocatalytic reduction of CO_2 to chemical fuels has attracted great attention because of its potentially high efficiency, feasibility and compatible integration with renewable energies (Zhang et al., 2018). Key products of CO_2 reduction with different equilibrium potentials are listed as Table 1.3 from CO at -0.11 V to CH_4 at $+0.16$ V *vs* RHE. The thermodynamic reversible potentials are close to each other and to that of water reduction, which suggests it is difficult to tune the catalytic selectivity by varying the reaction thermodynamics with applied potentials. CO_2 is an extremely stable molecular structure with two carbon-oxygen double bonds (Zhang et al., 2017), and strong activation energy is required to break the chemical bond in the reaction procedure. It is, therefore, necessary to develop efficient electrocatalysts to promote the sluggish kinetics of CO_2 reduction. Since various possible small carbonaceous molecules would be formed through different pathways, the choice of employed electrocatalyst and applied potential play a critical role in an efficient and selective CO_2 reduction (Torelli et al., 2016). Up to now, high-efficient, low-cost and long-term stability electrocatalysts are still to be discovered for use in a practical environment. In the past decades, considerable efforts have been devoted to overcoming the above obstacles and to meeting the requirements of the large-scale commercial application (Benson et al., 2009; Costentin et al., 2013; Wang et al., 2015). In this thesis, we investigated the electrocatalytic activity of CO_2 reduction performed by an intermetallic Cu-In-oxide.

Table 1.3 The possible reactions during the electrocatalytic CO_2 reduction (Benson et al., 2009; Hori, 2008)

Possible half-reaction of electrochemical CO_2 reduction	E^0 vs RHE	
$CO_2+2H^++2e^- \longleftrightarrow CO+H_2O$	-0.11 V	
$2H^++2e^- \longleftrightarrow H_2$	0.00 V	All values are close to the H_2 evolution potential (0.00 V)
$CO_2+6H^++6e^- \longleftrightarrow CH_3OH+H_2O$	$+0.02$ V	
$2CO_2+12H^++12e^- \longleftrightarrow C_2H_4+4H_2O$	$+0.07$ V	
$2CO_2+12H^++12e^- \longleftrightarrow C_2H_5OH+3H_2O$	$+0.08$ V	
$3CO_2+18H^++18e^- \longleftrightarrow C_3H_7OH+5H_2O$	$+0.09$ V	
$CO_2+8H^++8e^- \longleftrightarrow CH_4+2H_2O$	$+0.16$ V	
$O_2+4H^++4e^- \longleftrightarrow 2H_2O$	$+1.23$ V	

$E^0_{H^+/H_2}$, $E^0_{CO_2/fuel}$, $E^0_{O_2/H_2O}$

E (V vs RHE)

1.6 Scope of this thesis

The aim of this thesis is to develop and understand inexpensive, stable and efficient alternative electrocatalysts replacing noble metal and its compounds for alkaline water splitting and CO_2 reduction. The combination of electrochemical characterizations and *in-situ* Raman measurements is used to analyze the formation of the interfacial active species under various applied potentials and provides detailed information about the reaction mechanisms for OER and HER under alkaline water splitting.

   Paper I studies the effect of pH value for the growth conditions of the synthetic precursors for the crystal growth orientation of the resulting NiO nanoflakes (NFs) and their OER activities under alkaline conditions. **Paper II and III** investigate the influence of Fe incorporation in NiO nanosheets (NSs) for both OER and HER properties of alkaline water splitting. *In-situ* Raman and electrochemical impedance spectroscopy (EIS) are applied to understand the real active species and the reaction mechanisms. **Paper IV** reports the self-optimization of NiFe layered double hydroxide (LDH) NSs during vigorous water electrolysis in alkaline media and investigates the influence on OER and HER activities. Various *ex-situ* and *in-situ* characterizations are utilized to uncover the reaction mechanism and probe the real active species during overall water splitting. The system is shown to work as a bi-functional HER and OER catalyst with between 83-95% electricity-to-fuel conversion efficiency with respect to the lower heating value of hydrogen.

   Paper V aims to design a stable and efficient electrocatalyst based on Cu_2O thin film for CO_2 reduction. *In-situ* Raman spectroscopy is carried out to monitor the dynamic formation of catalytically active mixed metal oxide $CuInO_2$ nanoparticles during the catalysis.

2. Experimental methods

2.1 Chemical synthesis

2.1.1 NiO nanoflakes

Hydrothermal method is a commonly used approach to synthesize nano-materials with a variety of morphologies (Rao et al., 2017). In **Paper I**, NiO NFs were prepared with the hydrothermal method with an approach to attain a tunable crystal growth orientation and microstructure formation. The NiO NFs were prepared by dissolving 0.03 M of $Ni(NO_3)_2 \cdot 6H_2O$ in 50 mL of mixed 2-propanol and deionized water (DI) water solution (volume ratio 1:1) under 30 min ultrasonication. Ammonia solution ($NH_3 \cdot H_2O$, 25%) was then slowly added into the prepared solution to tune the pH value under stirring for 1 h. The as-obtained precursor was transferred to a 100 mL Teflon-lined stain-less-steel autoclave, heated to 180 ^{o}C with a heating rate of 5°C min^{-1} and kept at 180 ^{o}C for 2 h in air conditions. After 2 h reaction, the oven was naturally cooled down to the room temperature. The reaction product was collected after cleaning by DI water and ethanol 3 times and drying at 80 ^{o}C in an oven for 12 h. Finally, the as-obtained materials were annealed to 350 ^{o}C with a heating ramp of 5 ^{o}C min^{-1} and kept it for 3 h under pure Ar environment (100 SCCM) to obtain the NiO NFs.

2.1.2 Fe doped NiO nanosheets/Ni foam

Chemical bath deposition (CBD) is among the simplest method for the fabri-cation of large-area nanomaterials from solution (Nair et al., 1998). All mate-rials studied in **Paper II** and **Paper III** were prepared by a facile CBD method. Ni foam was immersed in a 3 M HCl solution for 30 min to remove the pos-sible surface oxide layer and subsequently washed by Milli-Q water (18.2 MΩ·cm at 25 °C) and absolute ethanol. The typical CBD procedure proceeded as follows; 0.5 g of poly(vinyl alcohol) (PVA) was dissolved in 40 mL of Milli-Q water at 90 ^{o}C under vigorous stirring. For Fe doped NiO NSs on Ni foam, 0.12 M of $Fe(NO_3)_3 \cdot 9H_2O$ and 1 M of $Ni(NO_3)_2 \cdot 6H_2O$ were added into the 40 mL of Milli-Q water as well to form a clear precursor. Next, a piece of the as-prepared Ni foam was immersed in the precursor solution. After 8 h of reactions at 85 ^{o}C, the Ni foam was taken out and cleaned by Milli-Q water to

remove residual reactants on the surface and then annealed at 550 $^\circ$C with a heating rate of 5 $^\circ$C min^{-1} for 3 h under ambient air conditions. For comparison and investigation of the effect of iron, NiO NSs on Ni foam was prepared by the same process without iron salt in the precursor solution during 12 h.

2.1.3 NiFe layered double hydroxide

Ultrathin NiFe LDH in **Paper IV** were synthesized by the hydrothermal method, growing directly on a three-dimensional substrate of Ni foam. In a typical synthesis, a piece of Ni foam (~2.5 cm × 3 cm) was immersed into 3 M HCl under 35 min of ultrasonication to remove any thick NiO$_x$ surface layer, if present. After 6 min of ultrasonic cleaning in DI water and absolute ethanol, respectively, the Ni foam was taken out and blown dry with compressed nitrogen. In the meantime, 0.29 g of Ni(NO$_3$)$_2$·6H$_2$O, 0.4 g of Fe(NO$_3$)$_3$·9H$_2$O and 0.6 g of CO(NH$_2$)$_2$ were dissolved into 80 ml of DI water under magnetic stirring for 30 min to form a homogeneous mixed solution. The as-prepared mixed solution was transferred into a 100 ml Teflon-lined stainless-steel autoclave with Ni foam vertically immersed into the solution with the topside protected using a Kapton tape. After *in-situ* growth in an autoclave at 120 °C for 12 h in an oven, the autoclave was cooled overnight down to the room temperature by the natural cooling procedure after turning off the oven. Next, the Ni foam was taken out and ultrasonically cleaned by DI water and ethanol for 6 min successively to remove any possible residual reactant on the surface and dried at 80 $^\circ$C for 12 h in an oven under ambient atmosphere. Ni(OH)$_2$ in **Paper IV** was prepared by the same procedure but without 0.4 g of Fe(NO$_3$)$_3$·9H$_2$O. The activated LDH catalysts, H-NiFe LDH, and O-NiFe LDH, were obtained after 100 h aging process *via* a two-electrode system with an applied potential of 1.7 V in 1.0 M KOH, corresponding to the cathodic reaction and the anodic reaction, respectively, at each side.

2.1.4 Cu$_2$O thin films

The nanostructured Cu$_2$O (**Paper V**) thin films were prepared by electrochemical deposition method in an alkaline solution of lactate-stabilized copper sulfate (Paracchino et al., 2012). The electrodeposition substrates, Fluorine-doped tin oxide (FTO, TEC 15 from Pilkington) and FTO coated with ~800 nm of Indium tin oxide (ITO) layer, were annealed at 500 $^\circ$C for 30 min. The ITO layer was deposited by a doctor-blade method using an ITO paste prepared by mixing 1 g of ITO powder ((Nano In$_2$O$_3$-SnO$_2$ Powder, 99.99%, In$_2$O$_3$:SnO$_2$=90:10, 20-40 nm, Inframat Advanced Materials), 3.2 g of terpineol containing 10 wt% ethyl cellulose and 0.2 mL of acetic acid in 11 mL of ethanol. The plating solution was comprised of CuSO$_4$ (0.2 M) and lactic acid solution (3 M) in DI water with 0.5 M K$_2$HPO$_4$ buffer. 2 M KOH was added to adjust the bath pH to be 12. The Cu$_2$O thin films were electrodeposited

under Galvanostatic mode at a constant current density of -0.16 mA cm^{-2} for 150 min using an Autolab PST100N in a two-electrode electrochemical cell with a Pt mesh as the counter electrode. The thickness of the ITO layer and Cu_2O thin films were measured by a Dektak profilometer (VEECO/SLOAN DEKTAK 3, New York, US) respectively, determined to about 800 nm thickness. Following the composition of the substrate, the as-prepared electrodes were named as Cu_2O/FTO and Cu_2O/ITO/FTO.

2.2 Physical characterization

2.2.1 X-ray diffraction

X-ray diffraction (XRD) is a powerful nondestructive technique to obtain structural information, *e.g.,* crystalline structure, average grain size, crystal orientations (Kohli and Mittal, 2011), based on constructive interference of elastically scattered monochromatic X-rays. In a crystalline material, the atoms will be arranged periodically and infinitely in three dimensions to form a regularly repeating crystal lattice with a plane spacing of d. When d is close to the X-ray wavelength (λ), the X-rays are constructively diffracted by the repeated crystal lattice plane distances. As shown in Figure 2.1, the lattice spacing can be obtained from the path difference between two beams of wavelength undergoing interference using the Bragg equation, $n\lambda = 2dsin\theta$, where n is a positive integer denoting the diffraction order, λ is the wavelength of incident X-rays, d is the adjacent crystal plane spacing and θ is the angle between the incident X-ray and the reflecting lattice plane.
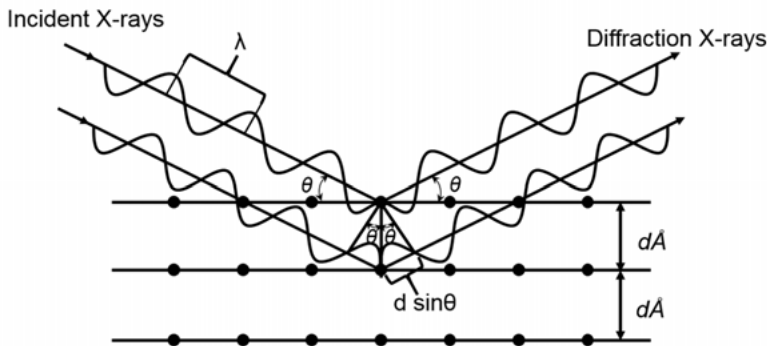

Figure 2.1 Schematic illustration of Bragg's Law and constructive elastic X-ray scattering.

In addition, XRD peaks broadenings from the lack of sufficiently repetitive lattice planes can be used to evaluate the mean size of nanometer-sized

particles or crystallites by using the Scherrer equation. The Scherrer equation can be expressed as

$$\tau = \frac{K\lambda}{\beta cos\theta} \qquad\qquad (2.1)$$

where τ represents the mean size of the crystallite, λ is the incident wavelength of X-rays, β is the 'width' with the definition as the full width at half maximum (FWHM), and θ is the Bragg angle as mentioned above, K is a shape factor with a typical value of about 0.9 for spherical particles. In addition, the actual value of K is dependent on at least three factors: the crystalline shape, the crystallite-size distribution, and the definition of the 'width'. If crystallites have the same assumed spherical shape, then the $K=0.9$ value can be applied, if it contains different shapes, a modified value must be used.

In Paper I and **II**, XRD measurements were carried out with a Bruker D8 Advanced diffractometer using Cu $K\alpha$ radiation (λ = 0.15418 nm). In **Paper IV**, XRD was performed with a Siemens D5000 Diffractometer in the parallel beam geometry using an X-ray mirror and a parallel plate collimator of 0.4°. The diffractograms were collected under Cu $K\alpha$ radiation (λ = 0.15418 nm) with 2θ ranging from 20° to 85° (0.05° per step) and 1° incidence angle. In **Paper V**, XRD was measured using a Philips PW1710 powder diffractometer (Philips, Amsterdam, Netherlands) and Cu Kα radiation (λ = 0.15418 nm) and step size of 0.015°. XRD was performed to identify the crystalline phase of the samples, growth orientation, and as a mean of determining the average crystalline grain size.

2.2.2 Electron microscopy

Scanning electron microscopy (SEM) and transmission electron microscopy (TEM) are the two most commonly used microscopic techniques to visualize the material structure, and in the latter case, also the crystalline diffraction (Thompson and Cheng, 2011). The surface morphology and elemental distribution in samples were measured by Zeiss 1550 operating at an accelerated voltage of 5-10 kV with secondary electron and Energy-dispersive X-ray spectroscopy (EDS) detectors. TEM, high-resolution transmission electron microscopy (HRTEM), and selected area electron diffraction (SAED) were carried out to further verify the material structure on a JEOL JEM-2100F microscope operated at 200 kV, equipped with a Gatan Ultrascan 1000 CCD camera, Gatan STEM BF/DF detectors, and a post-column energy filter (GIF Tridiem). The probe size and camera length were set to be 0.5 nm and 2 cm, respectively. The probe size and scanning rate were optimized to minimize beam damage and to obtain a reasonably good signal-to-noise ratio. Since TEM images are constructed from the transmitted electrons, often ultrathin slices or particles of dimensions less than 100 nm are required. In **Paper I**, TEM samples were prepared by sonicating NiO NFs powders in ethanol and

drying a droplet of the suspension onto carbon supporting film of the TEM grids. In **Paper II and IV**, because the synthesized materials were *in-situ* growth on the substrate of Ni foam, the TEM specimens were scratched off from the surface of the as-prepared samples by a diamond scriber onto a TEM grid with holey carbon supporting films.

2.2.3 Zeta potential—pH titration

Zeta potential is the charge formed at the interface (Helmholtz layer) between the solid surface and the liquid medium. In the Stern-Graham model, the Helmholtz layer is divided into two parts: an inner layer with ions that are relatively tightly bound to the surface and outer layer where the difference between electrostatic forces and random thermal motion determines the ion distribution.

The pH environment is an essential factor for the surface zeta potential value, as most surfaces and macromolecules are charged in solution due to hydrolysis, protonation/deprotonation or other ion exchange reactions. When the surface charge turns to zero at a specific pH, this pH is defined as the point of zero charge (PZC), playing an important role on the protonation-deprotonation behavior for (hydr)oxides in aqueous suspensions related to the crystalline growth and aggregation (Bourikas et al., 2005). In **Paper I**, PZC of NiO was measured on a Zetasizer Nano ZSP equipped with an MPT-2 Autotitrator (Malvern instruments) by using electrophoretic dynamic light scattering with the salt addition method using either 0.1 M or 0.25 M of NaCl water solution at the room temperature. NiO powder (0.1 g) were dispersed in 20 mL with two different concentrations of NaCl water solution under 30 min ultrasonication, then transferred to a folded capillary cell (DTS1070) with gold electrodes. The pH of the suspension was adjusted by 0.25 M, 0.01M of NaOH and 0.25 M of HCl where bubble formation was avoided by using a connected degasser during the measurements. The addition of different concentrations of NaCl was to improve the solvent conductivity and verified to not affect the PZC of the NiO.

2.2.4 X-ray photoelectron spectroscopy

X-ray photoelectron spectroscopy (XPS) is a classical surface-sensitive analytical technique for the surface elemental composition and chemical states information (Mather, 2009). In principle, mono-energetic Al Kα or Mg Kα excites the element core level electrons at the sample surface causing photoelectrons to be emitted from the surface to the vacuum state, as shown in the schematic representation in Figure 2.2. By detecting the kinetic energy (KE) of the emitted electrons, it is possible to identify the surface elements and chemical states. Using Koopmans' theorem (Koopmans, 1934), the binding energy (BE) can be extracted by the simple equation $BE = hv - KE$ and peak

intensities, the detected components can also be quantified. In this thesis, XPS was mainly used to compare the elemental composition and metal oxidation states before and after electrocatalysis. The data were obtained by a PHI Quantum 2000 and Perkin Elmer PHI 5500 spectrometer using monochromated Al Kα radiation (1486.6 eV) with a 45° angle of photoelectron emission. The detailed parameters are set based on the unique property of samples and measurement requirements. For example, electron neutralization and ion gun neutralization were used for charge compensations in **Paper II and IV** because of the limited conductivity of as-prepared samples. All spectra were analyzed in the CasaXPS software and were calibrated before the analysis.
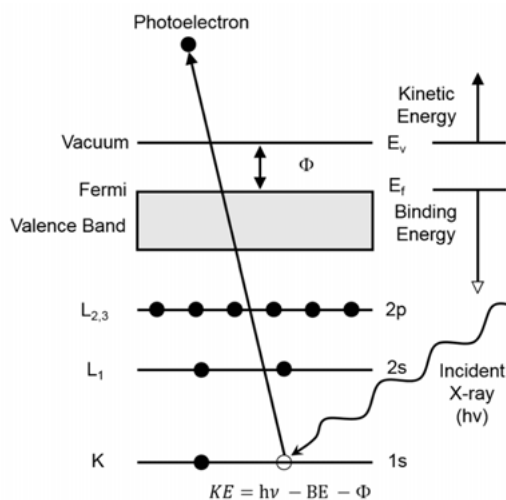
Figure 2.2 Schematic illustration of the photoemission process involved in XPS surface analysis. Φ is the work function, determined by the property of the spectrometer and samples.

2.2.5 Raman spectroscopy

Raman spectroscopy is a powerful analytical technique based on inelastic scattering from the sample using a monochromatic light from a laser beam and gives information about transitions between rotational and vibrational states. Raman spectroscopy can be used for analysis of bonds and functional groups (Socrates, 2004; Yang et al., 2005), crystallinity and crystalline phase determination (Kosacki et al., 2002; Ledinský et al., 2006; Naylor et al., 1995; Strobl and Hagedorn, 1978), orientation of crystals and surface molecules (Basova and Kolesov, 1998), molecular interactions and defects in solids (Campion, 1985), low frequency excitations (magnons, plasmons) (Birman et al., 1979), as well as more exotic phenomena such as broken symmetry (Cépas et al., 2008; Osada et al., 1999) and spin-phonon coupling (Laverdière et al.,

2006; Lockwood and Cottam, 1988). This approach does not require any specific sample preparation and can be used for vibrational characterization of molecules, liquids, and solids and is unique in the sense that it can detect many different aggregation states and forms of matter simultaneously where intermediate amorphous states, potential molecular or cluster species, molecules, molecule interaction, and recrystallization status can be monitored (Jain et al., 2016). When the laser is irradiated onto the sample, a small portion of the photons in the laser can lose some of the energy to excite a vibration level in the material, if the polarizability (α) of the electron cloud is changed during the vibration. The interaction of light with the chemical bond in the sample with changed polarizability, cause inelastic scattering with a result that the photon frequency is shifted up or down. The polarizability is formally a tensor but for an isotropic material and polarized light can be defined as the resistance to create a dipole (μ) with a given electric field (E) with $\mu=\alpha E$, where the polarizability during a small nuclei displacement, z_0, in an oscillating field can be Taylor expanded and described by

$$\alpha=\alpha_0+\left(\frac{\partial\alpha}{\partial z}\right)_0 z+... \qquad (2.2)$$

where α_0 is the displacement independent polarizability and $(\partial\alpha/\partial z)_0$ is the change in polarizability during bond displacement in the z-direction. Fixing the coordinate system so that the polarized light is probing the displacement in the z-direction, and denoting the frequency of the light v_0 and the material vibration frequency v_M, considering only the time-dependent part of the electric field at a fixed location, $E=E_0\cos(2\pi v_0 t)$ and recalling that $\mu=\alpha E$, one can write (Ferraro, 2003)

$$\mu=\alpha_0 E_0 \cos(2\pi v_0)+\frac{1}{2}\left(\frac{\partial\alpha}{\partial z}\right)_0 z_0 E_0 \cos[2\pi(v_0+v_M)t] +\frac{1}{2}\left(\frac{\partial\alpha}{\partial z}\right)_0 z_0 E_0 \cos[2\pi(v_0-$$
$$v_M)t] \qquad (2.3)$$

where the first term is the dipole that contributes to the elastic (Rayleigh) scattering, the second term to the anti-Stokes inelastic scattering and the third to the Stokes inelastic scattering. The scattered field can then be extracted from the acceleration of the dipole *via* the second time derivative using conventional classical electrodynamics, while the properties of α for a given molecule or crystal vibration require a quantum mechanical description to correctly account for the orbital density change during a vibration.

The energy difference between the incoming and the inelastically scattered light (Raman shift) of a scattered photon can be expressed as a relative change in frequency with

$$\Delta\sigma=\frac{1}{\lambda_{incident}}-\frac{1}{\lambda_{scattered}} \qquad (2.4)$$

where $\Delta\sigma$ is the wavenumber defined by $\sigma = v/c$, v is the frequency and c is the velocity of light (about 3×10^{10} cm/s). If the energy of the scattered photons is lower than the energy of the excited photons as found in the third term in Eqn. 2.3, the scattering light is called Stokes line, which is the common inelastic scattering to analyze in Raman spectroscopy. For an increase in frequency, the anti-Stokes line occurs and is weaker in intensity. A comparison of their transitions in an energy level diagram is shown in Figure 2.3. At room temperature, the Raman spectrum of anti-Stokes scattering is always weaker than the Stokes scattering spectrum as most materials have a dominating fraction in their vibrational ground state, therefore, most Raman experiments only consider Stokes scattering. The anti-Stokes spectrum will be more pronounced at higher temperatures or for vibrations involving heavier elements but can be used when fluorescence is a problem at the Stokes side or if the temperature of the sample under the laser light is desired to be characterized.
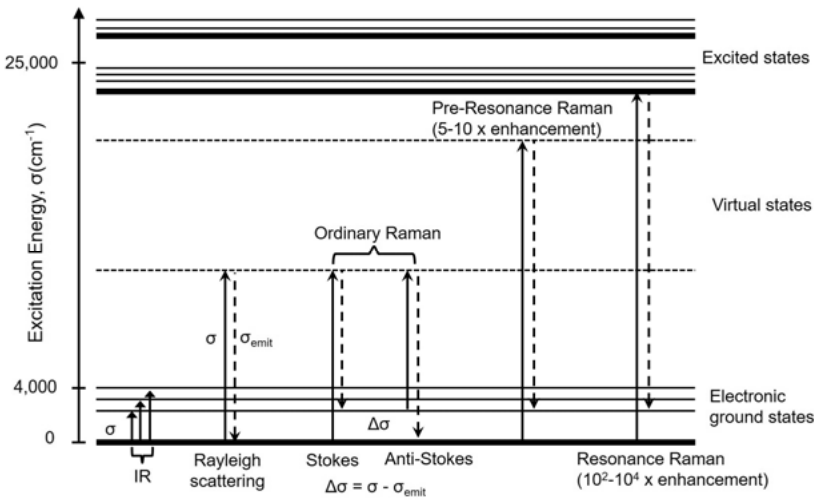
Figure 2.3 Energy level diagram for the transition involved in IR absorption, Rayleigh, and Raman scattering processes.

The frequency shift of the incoming light comes from excited vibration energies specific for each bond type. In this thesis, the Raman spectrum was collected by a confocal Raman microscope (RM 1000, Renishaw) at ambient conditions. The as-prepared samples were irradiated by a green laser source of 532 nm (doubled Nd: YAG laser) with 2–10 mW laser power. All Raman spectra were recorded using a1800 lines/mm grating that together with the distance to the CCD detector, resulted in a resolution of $\sim$1 cm^{-1} and calibrated to the value of $\sim$520.5 cm^{-1} of a silicon wafer. Based on the specific band feature, it enables characterization of the vibrations in the materials and by such the material presence, structure and crystalline phase.

2.3 Electrochemical characterization

For water splitting, all electrochemical measurements were performed in 1 M KOH or NaOH (degassed with N_2 for 2 h before measurements) on a CHI760C electrochemical workstation or Zahner workstation at room temperature. The corresponding current density was normalized to the geometrical area of electrodes. The overall water splitting was performed in a two-electrode configuration, while the half-cell studies were carried out in a three-electrode system, using a Pt mesh (wire) as a counter electrode, Ag/AgCl (1M or 3M KCl) as a reference electrode and synthesized materials as the working electrode. A glass frit separated the working electrode and the counter electrode. Different techniques were used to quantify the catalytic properties of the prepared electrocatalyst materials. For comparisons, the measured potential was converted to RHE scale, following the equation:

$$E_{RHE} = E_{measured} + E_{Ag/AgCl} + 0.059 \times pH \ (pH = 14 \pm 0.2) \qquad (2.5)$$

It is noteworthy that the equilibrium potential of the electrodes changes with pH, and their relationship can be expressed as Eqn. 2.6, which is reflected in Eqn. 2.5.

$$E_{rev} = E^0 - 0.059 \times pH \quad (25\,^{o}C) \qquad (2.6)$$

For water electrolysis, the reversible thermodynamic potential against pH is shown in Figure 2.4. When the applied potential is between 0 and 1.23 V, there is no enough driving force to generate O_2 and H_2. This region can be used to investigate the interaction between electrode and electrolyte. When the driving energy is enough to pass the barrier, the gas evolution will start.
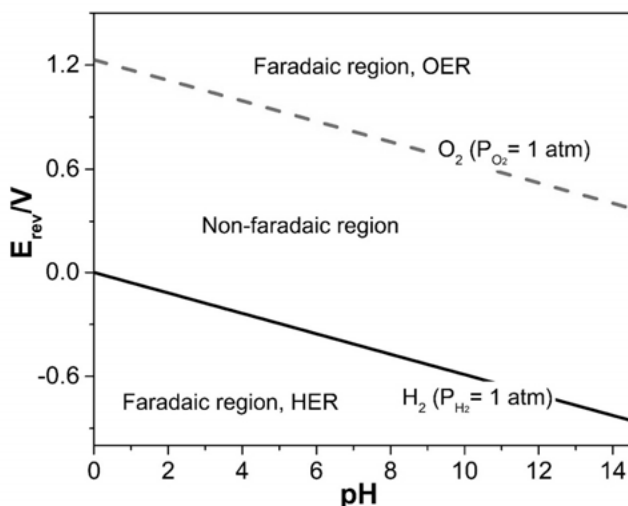
Figure 2.4 Reversible thermodynamic potential of water electrolysis at 25 ^{o}C, 1 atm.

The overpotential η for cathodic HER and anodic OER in alkaline media is defined as below:

$$4e^- + 4H_2O \Leftrightarrow 4OH^- + 2H_2 \qquad \eta_{cathode} = E_{RHE} - 0 \ V \qquad (2.7)$$

$$4OH^- \Leftrightarrow 2H_2O + 4e^- + O_2 \qquad \eta_{anode} = E_{RHE} - 1.23 \ V \qquad (2.8)$$

For CO_2 reduction, all electrochemical measurements were performed with a three-electrode configuration using Autolab PST100N chemical workstation, where a Pt mesh and an Ag/Ag^+ (0.1 M $AgNO_3$ in acetonitrile) were used as a reference and counter electrode, respectively. The prepared electrolyte (0.1 M Bu_4NPF_6 in acetonitrile) was degassed with Ar (Carbagas 99.998%) for 15 min to remove O_2 before starting measurements. The measurements were performed under CO_2 saturation condition.

EIS was used to study the charge-transfer mechanism involved in the multistep Faradic reaction for alkaline water splitting, measuring in a frequency (f) range from 1 Hz to 100 kHz using 5 or 10 mV amplitude alternating current (AC) potential at various applied direct current (DC) potentials. All EIS circuits were fitted by using the ZView software.

Ideally, electrical resistance R is defined as a ratio of the input voltage (V) to the output current (I) by the Ohm's Law:

$$R = \frac{V}{I} \qquad (2.9)$$

However, the real world contains resistance with a more complex behavior than the idea resistor, where electrical impedance is used to replace the electrical resistance to demonstrate not only the ability of a circuit to resist the flow of electrical current, denoted as the "real impedance" but also the ability of circuit to store electrical energy, represented by the "imaginary impedance".

In the experimental situation, EIS is typically measured at a constant direct current (DC) voltage with a superimposed alternating current (AC) voltage excitation signal V of a small amplitude V_0. An impedance spectrum is obtained *via* varying frequency (f) over a defined range to an electrochemical cell and then measuring the current through the cell. The alternating voltage V can be expressed as a function of time t as follow:

$$V(t) = V_0 \sin (2\pi ft) = V_0 \sin (\omega t) \qquad (2.10)$$

In a linear system, there is a phase (φ) shift and a different amplitude I_0, which can be expressed as:

$$I(t) = I_0 \sin (2\pi ft + \varphi) = I_0 \sin (\omega t + \varphi) \qquad (2.11)$$

The AC voltage input V and the response current signal I at a single frequency f. are shown in Figure 2.5.
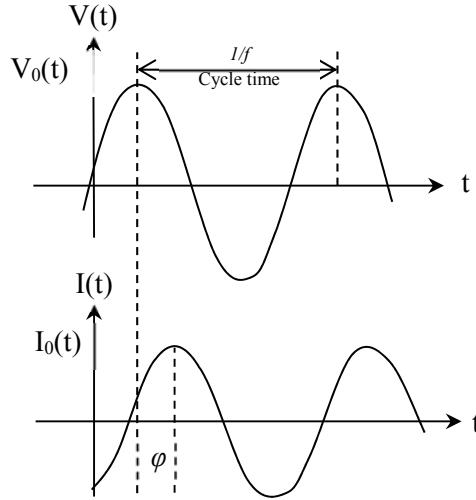

Figure 2.5 AC voltage input V at a single frequency f and the current response I passing through the sample.

An expression based on Ohm's law allows us to calculate the system impedance as:

$$Z = \frac{V_{(t)}}{I_{(t)}} = \frac{V_0 \sin(\omega t)}{I_0 \sin(\omega t + \varphi)} = Z_0 \frac{\sin(\omega t)}{\sin(\omega t + \varphi)} \tag{2.12}$$

The impedance is represented in terms of a magnitude Z_0, and a phase shift φ.

Eqn. 2.12 can also be expressed according to Euler's relationship as

$$exp(j\varphi) = cos\varphi + jsin\varphi \tag{2.13}$$

where φ is a real number and j is the imaginary unit, $j^2 = -1$.

The potential $V(t)$ and the current response $I(t)$ can be described as a complex function as Eqn. 2.14 and 2.15.

$$V(t) = V_0 \, e^{j\omega t} \tag{2.14}$$

$$I(t) = I_0 \, e^{j\omega t + j\varphi} \tag{2.15}$$

AC impedance subsequently formulated as

$$Z = \frac{V_{(t)}}{I_{(t)}} = \frac{V_0}{I_0} e^{-j\varphi} = |Z_0| e^{-j\varphi} \tag{2.16}$$

where $-\varphi$.is the phase angle.

40

By a Fourier transform, the function of time $F(t)$ can be converted into a function of frequency $F(\omega)$.

$$F(\omega)=\int_0^T f(t)e^{-j\omega t}dt \tag{2.17}$$

One can now define the conventional impedance $Z_{(\omega)}=V_{(t)}/I_{(t)}$, the magnitude is $|Z_{(\omega)}|=|Z_0|$ and the phase angle is $-\varphi_{(\omega)}$
According to Euler's equation (2.13), Eqn. 2.16 can be expressed as

$$Z_{(\omega)}=|Z_0|(cos\varphi - jsin\varphi)=Z_{Re} - jZ_{Im} \tag{2.18}$$

where the real part of impedance is the resistance Z_{Re}, and the imaginary part is the reactance Z_{Im}.

There are two types of reactance, inductive and capacitive. The reactance of an inductive element is ωL, where L is the inductance and $\omega = 2\pi f$. The reactance of a capacitive element is negative, $-1/\omega C$, where C is the capacitance. The negative sign occurs because the impedance of a pure capacitor is $1/j\omega C$ and $1/j = -j$.

Besides impedance, admittance, Y, can be also used to investigate the electrical properties of materials, which is the reciprocal of impedance.

$$Y_{(\omega)}=Y' - jY''=\frac{I_{(\omega)}}{V_{(\omega)}} = \frac{1}{Z_{(\omega)}} \tag{2.19}$$

where Y' is the conductance and Y'' is the susceptance.

The relationship between impedance and admittance involving resistance and inductance is given in Table 2.1.

Table 2.1 Impedance and admittance of three basic electrical elements

Elements	Symbol	Impedance	Admittance
Resistor	R	R	$1/R$
Capacitor	C	$-j/\omega C$	$j\omega C$
Inductor	L	$j\omega L$	$-j/\omega L$

EIS is a useful technique to investigate interfacial reactions. For a simple electrochemical reaction $O+ne^- \rightarrow R$, the measurement is performed at a certain DC polarization steady state. In the measured frequency range, the equivalent circuit (EC) can be simplified as shown in Figure 2.6 only considering charge

transfer. This model was introduced in the journal of "Discussions of the Faraday Society" by Randles in 1947 (Randles, 1947).
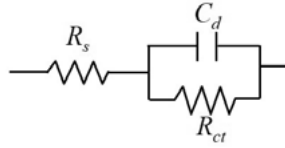
Figure 2.6 The EC of Randles's electrochemical cell.

In Randles's cell, C_{dl}, R_s, R_{ct} are referred to the double-layer capacitance, solution resistance, and charge/electron transfer resistance, respectively. Utilizing Randles's circuit, the impedance can be expressed as a function of frequency with

$$Z(\omega)=R_s+\frac{R_{ct}}{1+\omega^2 R_{ct}^2 C_{dl}^2}-\frac{j\omega R_{ct}^2 C_{dl}}{1+\omega^2 R_{ct}^2 C_{dl}^2} \tag{2.20}$$

where the real part of impedance (Z') is given by

$$Z'(\omega)=R_s+\frac{R_{ct}}{1+\omega^2 R_{ct}^2 C_{dl}^2} \tag{2.21}$$

and the imaginary part (Z'') is

$$Z''(\omega)=-\frac{\omega R_{ct}^2 C_{dl}}{1+\omega^2 R_{ct}^2 C_{dl}^2} \tag{2.22}$$

In **Paper III**, we used two different ECs (Figure 2.7) to model the OER and HER processes based on an extension of ECs proposed by Harrington and Conway (HC) (Harrington and Conway, 1987), respectively.
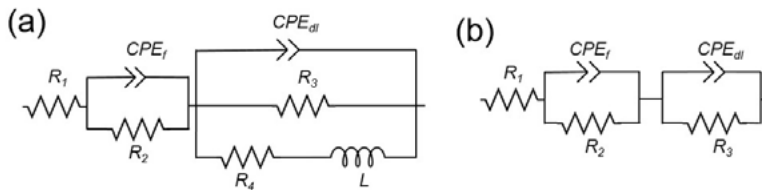
Figure 2.7 Two possible ECs of (a) abbreviated L-CPE, including an inductive response at low-frequency range and (b) abbreviated 2R-CPE, including constant phase elements describing the ac impedance response during the reaction.

These two ECs are used to model the catalytic behavior on Fe-NiO NSs on Ni foam for alkaline water splitting. In the circuit of *L-CPE*, R_1 is the series resistance, CPE_f–R_2 is the quasi-ideal behavior of porous electrode, CPE_{dl}–R_3 in parallel of *L*–R_4 represents the electrode charge transfer behavior. The inductive behavior is dependent on the surface coverage changing. The *2R-CPE*

model consists of a series resistance (R_1), quasi-ideal dielectric capacitance CPE_f in parallel of a film resistance R_2, surface charging constant phase element CPE_{dl} in parallel of a reaction resistance R_3.

In EIS experiments, capacitors often do not behave ideally and for these cases can be replaced by a constant phase element (CPE) defined *via*

$$Z_{CPE} = \frac{1}{(j\omega)^{\alpha}Q} \tag{2.23}$$

where α is the constant phase exponent, ω is the angular frequency of the sinusoidal applied potential, Q is a constant, related to the electrochemical double layer capacitance. When $\alpha = 1$, Q represents the capacitance of the interface with units of F/cm^2. When $\alpha < 1$, the system shows non-ideal capacity behavior at the interface, which is commonly attributed to surface heterogeneities (Birla Singh and Kant, 2014) or to continuously distributed time constants for charge-transfer reactions (Drüschler et al., 2010). It is clear that the parameter Q of CPE cannot represent the capacitance when $\alpha < 1$.

Therefore, the impedance related to a simple Faradaic reaction without diffusion in Figure 2.6 can be expressed in terms of a CPE as

$$Z_{\omega} = R_s + \frac{R_{ct}}{1 + Q(j\omega)^{\alpha}R_{ct}} \tag{2.24}$$

where R_s is the Ohmic resistance and R_{ct} is the charge-transfer resistance.

2.4 *In-situ* Raman spectroscopy

Potential dependent Raman spectra were measured on a custom-made spectro-electrochemical cell as shown in Figure 2.8.
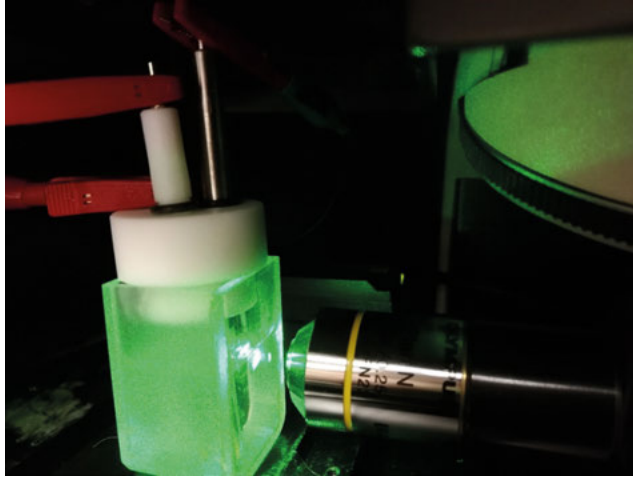
Figure 2.8 Experimental setup for potential dependent Raman measurements.

In this thesis, *in-situ* Raman results constitute an important approach to revealing the active surface species transformation during catalytic reactions. All spectra were collected during a current-time (I-t) measurement at different constant electrochemical potentials. The duration time was about 30 min to ensure that the Raman bands were recorded under the steady-state reaction at each potential. A confocal Raman microscope with a 90-degree angled Olympus lens with 10 times magnification and a quartz cell standing in front of the objective lens was used (Figure 2.8). Green laser radiation (532 nm) was focused on the prepared working electrode and each spectrum was recorded with 10 s acquisition time for 10 sweeps. All spectra were normalized based on the peak of ~140 cm^{-1}. Other details of the setup and spectral shift calibration are the same as used in the regular Raman measurements.

3. Results and discussion

In this chapter, the major findings from the appended papers are presented as a concise summary, which will focus on two parts, Ni-based electrocatalysts for alkaline water splitting and Cu-based mixed metal oxide electrocatalysts for CO_2 reduction.

3.1 Ni-based electrocatalysts for alkaline water splitting

In the past decades, Ni-based electrocatalysts have attracted increasing attention for alkaline water splitting because of their low cost, excellent stability and good catalytic activity (Vij et al., 2017). Moreover, because Ni is standing at the same group with the high catalytic performance Pt in the periodic table, the electronic properties of Ni-based materials for catalytic applications have also aroused the great interest of many researchers (Landon et al., 2012). In **Paper I**, we investigated how to adjust the morphology of NiO nanomaterials to obtain an improved effect on OER performance. Except for increasing the active surface area, sufficiently high electrical conductivity is also a significant factor for electrochemical reactions driven by electrocatalysts (Qiu et al., 2014). As we know, pure stoichiometric NiO crystals exhibit very low p-type conductivity with a wide band gap of 3.6–4.0 eV (Joshi et al., 2006), which poses some limitations in its electrochemical applications (Cheng and Jiang, 2015). Notably, its resistivity can be lower by transition metal doping into NiO lattice (Yan et al., 2016). Given many previous reports (Fominykh et al., 2015; Li and Selloni, 2014; Pebley et al., 2017; Wu et al., 2018), the substitutional incorporation of Fe(III) into the NiO lattice is helpful to improve the catalytic property. In our work, we used a facile CBD method to synthesize Fe doped NiO NSs and investigate the catalytic property for alkaline water splitting. From *in-situ* Raman spectra and EIS results, we found that the presence of Fe plays a crucial role in the electrochemical activities to lower the activation energy (**Paper II and III**). *In-situ* Raman spectra reveal the active surface species of Fe-NiO NSs during water electrolysis are Ni(Fe)OOH rather than the starting oxides. NiFe LDH was developed to further explore the role of Ni and Fe for alkaline water splitting. The work in **Paper IV** examines the catalytic properties of NiFe LDHs and the active sur-

face phases for both OER and HER under alkaline conditions. The corresponding detailed discussions for the findings in the different papers are presented below.

3.1.1 Controllable crystal growth orientation of NiO NFs and their OER activities

A facile hydrothermal method was used to fabricate NiO NFs as shown in Figure 3.1, where the varied pH value was utilized to adjust the crystal growth direction of $Ni(OH)_2$ and in resulting NiO after annealing. We found that the self-assembled properties of NiO NFs critically depends on the balancing of forces during synthesis, which can be controlled by alteration of the surface charge through changing the reactive pH value.
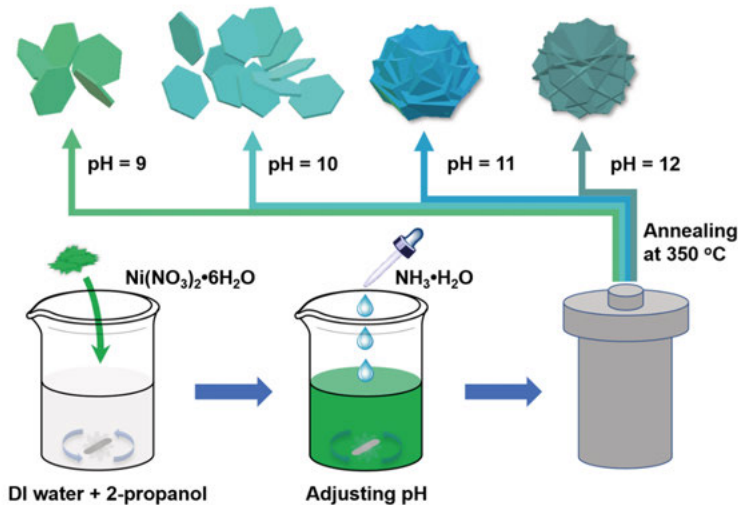
Figure 3.1 Illustration of NiO NFs fabrication with controllable morphologies by pH alteration around the PZC.

The XRD patterns of the NiO nanomaterials are consistent with cubic NiO (database: ICDD: 00-004-0835). Indexing of the diffraction peaks and comparing the relative intensities can then be utilized to analyze the crystal growth orientation. Note that as the materials are grown into aggregation, the peak intensities reflect both the extension of the NFs in themselves and the orientation of them in their microstructure, combined into the crystal growth orientation signal. As shown in Figure 3.2 and Table 3.1, it is clear that the crystal growth orientations along [111] and [220] are decreasing with increasing pH values with respect to the strongest diffraction peak orientation [200]. The average grain size of the prepared NiO NFs was quantified from the XRD peak broadening using the Scherrer's formula, neglecting strain, based on the strongest diffraction peak (200) in the plane of the NFs (Qiu et al., 2017) as

shown in Table 3.1. The result reveals that NiO NFs synthesized at pH 10 possess the smallest lattice extension about 6 nm in the [200] direction. TEM analysis (Figure 3.3) shows an extension of about 100 nm in the NFs with local (200) lattice diffractions in the plane of the NFs revealing that the NFs are polycrystalline, where the size of the polycrystalline domains and orientations are changing as a result of the pH adjustment. As seen in SEM images (Figure 3.4a-d), the surface morphology of the NiO nanostructure is affected by the adjusted pH values. The NiO prepared at pH 9 is composed of many individual pieces of NF, while the single NF aggregates to form uniform flower-like architectures when pH value is 11.
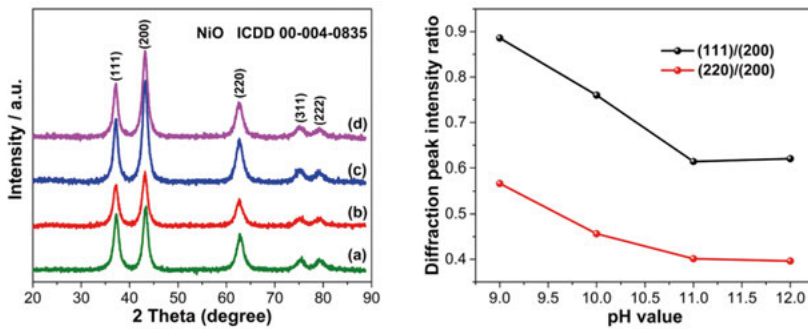
Figure 3.2 XRD patterns of as-formed NiO samples prepared at different pH values of (a) pH 9, (b) pH 10, (c) pH 11, (d) pH 12 and the relative intensity ratio of XRD peaks of (111) and (220) in comparison with that of (200).

Table 3.1 The average grain size of the synthesized NiO NFs in the [200] direction and relative peak intensity ratios of (111)/(200) and (220)/(200).

Sample NiO	Average grain size in [200] (nm)	(111)/(200) Intensity ratio	(220)/(200) Intensity ratio
pH= 9	6.5	0.886	0.567
pH=10	5.9	0.760	0.456
pH=11	7.9	0.614	0.401
pH=12	10.0	0.620	0.396
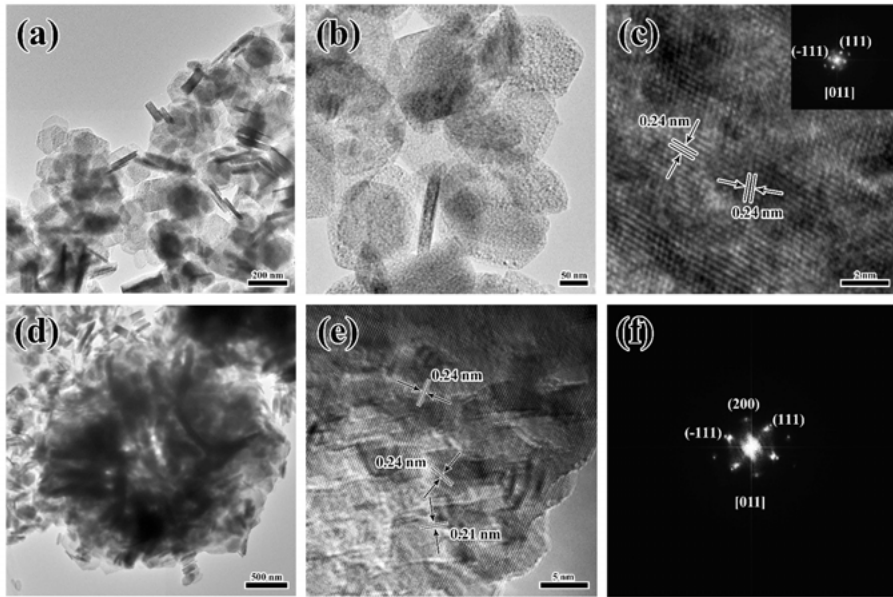
Figure 3.3 TEM, HRTEM images and the corresponding FFT of NiO NSs at pH 10.

As we know, the pH value plays a vital role for the surface charge and the specific pH value at the surface net charge of zero is an essential factor for the surface properties of metal oxides/hydroxides (Bourikas et al., 2005; Kosmulski and Science, 2002). The pH-dependent dissociation of the hydroxyl groups on the NiO surface is known to react *via* Eqn. 3.1:

$$NiO^- \underset{-H^+}{\overset{+H^+}{\Longleftrightarrow}} NiOH \underset{-H^+}{\overset{+H^+}{\Longleftrightarrow}} NiOH_2^+ \tag{3.1}$$
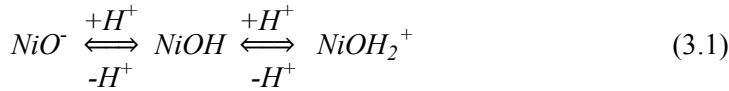
With the addition of ammonia, the above equilibria shift to the left with increased deprotonation, resulting in an increase of the negative net charge. The surface net charge will pass zero at a certain pH (Point of Zero Charge, PZC) and go to the negative net surface charge at higher pH values. As seen in Figure 3.4e, the measured PZC of commercial NiO is ~10.5 in NaCl (two different electrolyte concentration, 0.1 M and 0.25 M) at 298.15 K. Combined with the measured PZC and morphology changes of as-synthesized NiO NFs, it can be deduced that the negative surface net charge makes NiO NFs self-assembled more strongly compared to positive charge, revealing that the negatively charges likely are positioned at the edges in contrast to the positive charges mainly situated at the face, in similarity with the charge distribution in some clays (more details can be found in **Paper I**).
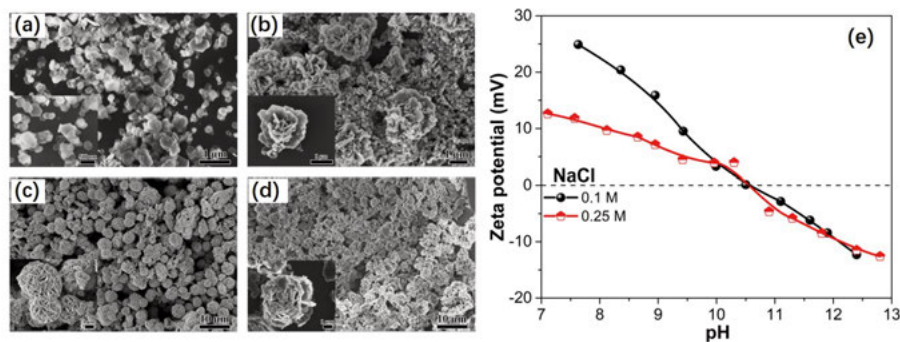
Figure 3.4 SEM images of the as-prepared NiO produced at (a) pH 9, (b) pH 10, (c) pH 11, (d) pH 12, (e) Zeta potential of NiO as a function of pH in two different concentrations of NaCl solution at 298.15 ±1 K.

The morphology and size of nanomaterials could directly affect their electronic, optical, magnetic, and catalytic properties (Daniel and Astruc, 2004; Zhao et al., 2009; Zhu et al., 2007). Figure 3.5 shows the electrochemical OER activity of the as-prepared NiO NFs on glassy carbon (GC). The OER activity of NiO NFs synthesized at pH 10 is markedly improved compared to the NiO NFs synthesized under other pH values (Figure 3.5a), which is mainly owing to its larger active surface area and lower reaction barrier. The prepared NiO at pH 10 possesses a minimal polycrystalline grain size in the grown irregulate NFs along with the direction of [200] and more exposed active site in the (0-11) planes, which would contribute to its catalytic performance. EIS plots (Figure 3.5b) indicate the reaction resistance of NiO pH 10 is the lowest among all formed NiO samples, which is in good agreement with its lower onset potential in Figure 3.5a. In summary, the OER activity of NiO NFs seems to be well correlated with the polycrystalline grain size and the NF surface morphology, which can be controlled by the pH value of the precursor condition in the synthesis process.
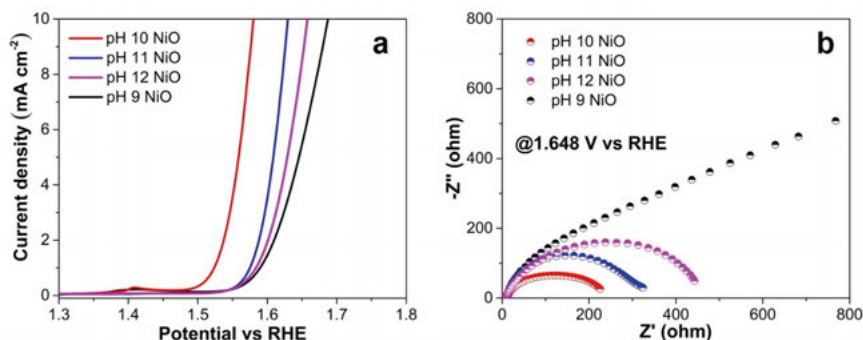
Figure 3.5 (a) Linear sweep voltammetry (LSV) curves of as-prepared catalysts in 1 M NaOH at low scan rates of 1 mV s^{-1} without iR compensation. (b) Nyquist plots measured at 1.648 V vs RHE.

3.1.2 Fe doped NiO NSs for enhanced OER and HER activities

Figure 3.6 shows a schematic illustration of the synthesis procedure of Fe doped NiO NSs on Ni foam (denoted Fe-NiO NSs) by a simple CBD method. The SEM images of prepared Fe-NiO NSs and corresponding EDS results are shown in Figure 3.7a-d, indicating that Fe is uniformly dispersed in the NiO NSs. The high-magnification SEM image (Figure 3.7e) gives a much clear view of the as-formed mesoporous NS arrays. As shown in the TEM micrograph in Figure 3.7f, the lattice spacing is 0.24 nm, well matched with the theoretical (111) interplanar spacing of cubic NiO (ICDD: 04-022-5465). There are no observed XRD peaks for any additional Fe compounds, while all diffraction peaks shift to the lower 2θ angle with the incorporation of Fe as seen in Figure 3.7g, indicating Fe ions were inserted into the NiO lattice and increasing the lattice spacing. The Fe-NiO NSs material composition and the effect from Fe incorporation are further confirmed by the Raman spectrum in Figure 3.7h. The broad Raman bands at ~508 and 1014 cm^{-1} observed in NiO NSs are shifted to the higher wavenumbers of ~550 and 1070 cm^{-1} with the presence of Fe, which is consistent with previous reports (Fominykh et al., 2015; Wu et al., 2018) and reveals higher frequency vibrations that would follow with a slightly weakened bonding strength or incorporation of a lighter element such as Fe, in comparison with Ni.
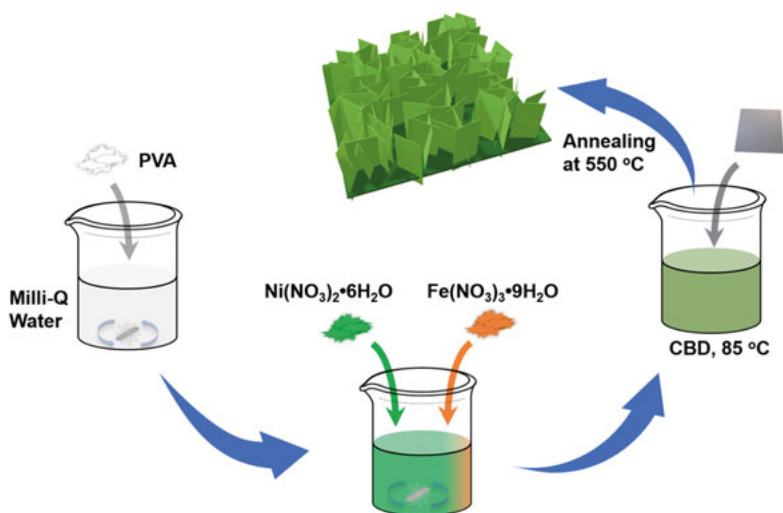
Figure 3.6 A schematic illustration of the preparation of Fe-NiO NSs on Ni foam.
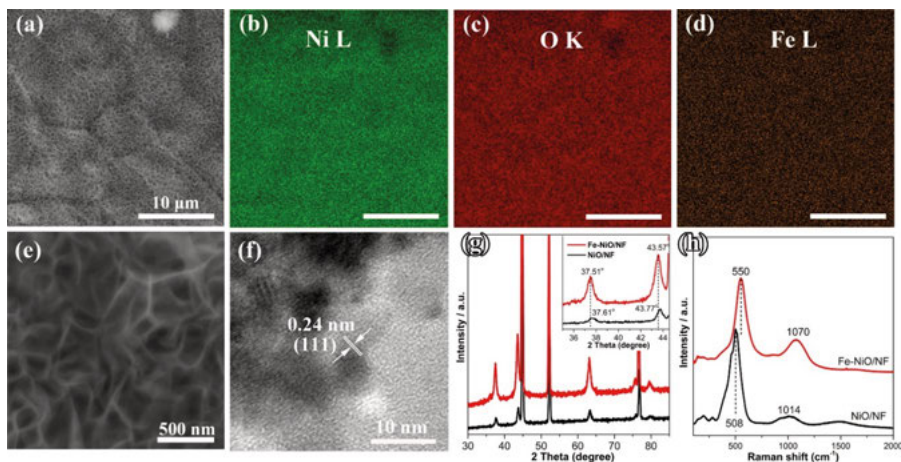
Figure 3.7 Material characterizations of the as-prepared catalysts. (a-d) SEM images and the corresponding EDS, (e) the high-magnification SEM image, (f) HRTEM image of Fe-NiO NS, (g) XRD patterns and (h) Raman spectra compared with Fe-NiO NSs and NiO NSs.

The Fe incorporation effect on the OER and HER performance were evaluated by LSV curves. As shown in Figure 3.8a, the Fe-NiO NSs on Ni foam require an anodic overpotential of 306 mV to reach 10 mA cm^{-2}, which is 55 mV less than that of NiO NSs on Ni foam. Utilizing Fe-NiO NSs as an electrocatalyst for the cathodic HER reaction, also shows an improved catalytic activity, with 183 mV η_{HER} to produce 10 mA cm^{-2} (Figure 3.8b). The electrochemical durability is an extremely important factor for a practical electrocatalyst. Current density-time (J-t) characterization shows that both of Fe-NiO NSs and NiO NSs deposited on Ni foam have stable activities for OER and HER at the same overpotential in the base solution, while Fe-NiO used as the surface electrode layer, exhibits better catalytic performance for the overall reaction (Figure 3.8c). These results show that Fe doping is beneficial for the catalytic property of NiO for alkaline water splitting and the catalytic improvement can be ascribed to the intentional incorporation of Fe rather than possible incidental impurities of Fe from the electrolyte. After identifying the OER and HER performance of Fe-NiO NSs and NiO NSs on Ni foam, the activities for the overall water splitting reaction were studied using the same electrocatalyst on both electrodes in a two-electrode configuration (Figure 3.8d). The results show a slight increase in the catalytic activity of NiO NSs for alkaline water electrolysis, likely from similar effects reported from Fe impurities in the electrolyte in previous studies (Klaus et al., 2015). Fe-NiO NSs only needs an applied potential of about 1.73 V to achieve the current density of 10 mA cm^{-2}, which is 124 mV lower than that of NiO NSs.
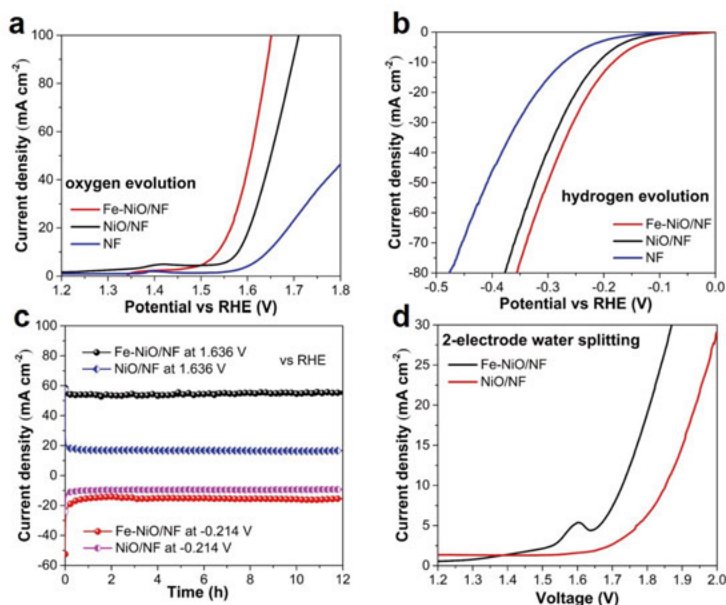
Figure 3.8 Electrochemical characterizations performed in 1 M N_2-saturated NaOH. LSV curves of (a) OER and (b) HER of Fe-NiO NSs, NiO NSs and Ni foam with a scan rate of 1 mV s^{-1} in a three-electrode system, (c) J-t tests of Fe-NiO NSs and NiO NSs at 1.636 and -0.214 V vs RHE, (d) polarization curves of Fe-NiO NSs and NiO NSs in a two-electrode system with a scan rate of 1 mV s^{-1}. The potentials are reported as measured, without iR corrections.

To figure out more detailed information about the processes, we used EIS and *in-situ* Raman spectroscopy to investigate the reaction mechanism and dynamics. Figure 3.9 shows the HER Nyquist plots performed at differently selected potentials from -1 to -1.4 V *vs* Ag/AgCl (3M KCl). The EIS curves (Figure 3.9b and d) show inductive behavior at large overpotentials in the low-frequency range, which means the dominating reaction for HER here is Volmer–Heyrovsky reaction since the Volmer–Tafel reaction cannot show inductive behavior as J.-P. Diard and co-workers reported (Diard et al., 1990). Nyquist plots of Fe-NiO NSs and NiO NSs for OER were measured in the same setup as that of HER under the selected applied bias from 0.3 to 0.7 V *vs* Ag/AgCl (3M KCl) as shown in Figure 3.10. In general, the EIS response of hydrous oxide film is expressed in three parts: electrolyte resistance, oxide film layer resistance in parallel with the film capacitance and interfacial reaction at the hydrous layer (Doyle and Lyons, 2013). The diameter of the semicircle with the real impedance axis at low-frequency can be interpreted simply as the interfacial charge transfer resistance. A smaller semicircle diameter implies a lower reaction barrier for the gas evolution. As seen in Figure 3.9 and 3.10, Fe-NiO NSs show a much smaller diameter of the semicircular arc during faradic reactions than that of NiO NSs, signifying that the Fe substitution in NiO NSs lowers the reaction barrier for both OER and HER. Even though EIS

52

curves provide some information in terms of the catalyst activity without adopting any EC, it is useful to have an EC whose elements can be assigned and interpreted as specific physical processes. This is possible as long as the processes are fairly well separated in the frequency domain. Given the observed inductive behavior in Figure 4.8, we adopt an extension of ECs proposed by Harrington and Conway (HC) (Harrington and Conway, 1987) to explore the underlying controlling factors for HER, which is *L-CPE* model. Another empirical EC containing two CPE is used to model their OER activity, which is the *2R-CPE* model. The difference between *L-CPE* and *2R-CPE* is the inductive element, which is observed in the EIS spectra during the HER process. However, even though EIS spectra of OER do not have the negative loop at low-frequency range, the quality of fitting is slightly better than that of *2R-CPE*, indicating OER process may also have an inductive behavior resulting from the coverage changing. As shown in Figure 3.10c, Fe-NiO NSs show a faster OER kinetic with a Tafel slope of 90.2 mV dec^{-1}, which is smaller than the value for NiO NSs (105.8 mV dec^{-1}) and bare Ni foam (151.3 mV dec^{-1}). In addition, the linear slope is obtained in the low overpotential and between the theoretical rate-determining values of Volmer step (120 mV dec^{-1}) and Heyrovsky step (40 mV dec^{-1}), which implies the combination of OH$^-$ with the metal site in forming MOH is the rate determining step (Bockris, 1956). For the HER process (Figure 3.10d), the Tafel slope of 105.5 mV dec^{-1} for Fe-NiO NSs is between the theoretical value signifying the Volmer (120 mV dec^{-1}) and Heyrovsky (40 mV dec^{-1}) steps, which further verify that Fe-NiO and NiO on Ni foam are proceeding *via* the Volmer–Heyrovsky reaction in alkaline solution. This is consistent with the reaction mechanism reported for NiO based catalysts in previous studies, e.g. by Shinagawa et al. (Shinagawa et al., 2015).
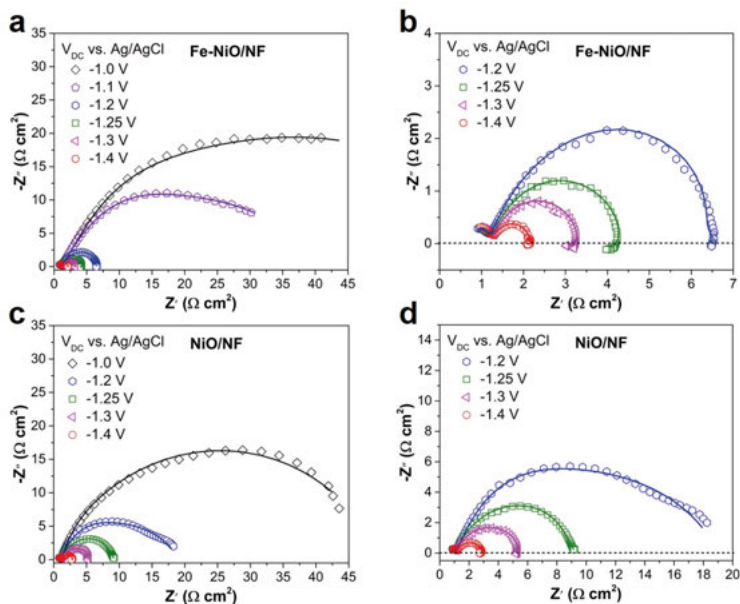
Figure 3.9 Nyquist plots of (a) Fe-NiO NSs, (c) NiO NSs and their corresponding magnification (b) and (d) for HER in a three-electrode system. EIS was measured in the frequency range of 1 to 10^5 Hz with 5 mV amplitude. The experimental points are shown by symbols and the fitting curves are presented by solid lines.
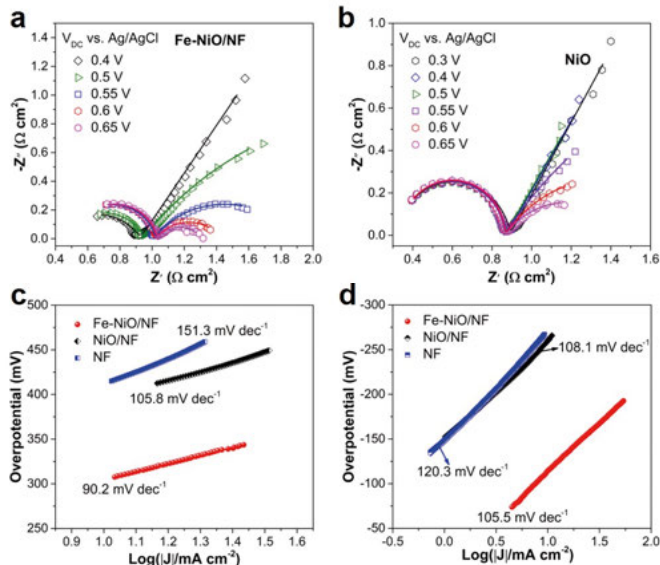
Figure 3.10 Nyquist plots of (a) Fe-NiO NSs and (b) NiO NSs for OER in a three-electrode system. Tafel plots of (c) OER and (d) HER. EIS was measured in the frequency range of 1 to 10^5 Hz with 5 mV amplitude. The experimental points are shown by symbols and the fitting curves are presented by solid lines.

In-situ Raman spectroscopy was utilized to obtain information about the surface active species transformation of $Fe_xNi_{1-x}OOH$. The Raman spectra show that the real active surface phases differ from the original phases and the reaction intermediates are altered as a function of the applied bias and material composition (Figure 3.11). With an applied negative potential *vs* RHE, the thermodynamic stability of the different phases change as known from normal Pourbaix diagrams, but also shifts the Femi level closer to the conduction band and change the ability for charge transfer. At the electrode surface, the hydroxyl groups are prone to attach to Fe^{3+} sites to form FeOOH with the Raman bands at 577 cm^{-1} and 690 cm^{-1}, which is consistent with vibrational assignments of FeOOH in iron oxide and hydroxide materials (De Faria et al., 1997). A more rapid or sluggish formation of these bands will then signify if the applied potential increase or decrease the ability to form the hydroxide with respect to the applied potential. The hydrogen group instead shows a tendency to adsorb on Ni sites ($Ni^{\delta+}-H_{ad}$ is shown at 750–950 cm^{-1} marked as a grass-green circle) at a more negative potential, which leads to the accelerated decomposition of water and thus enhances their HER activity. Moreover, the Fe incorporation promotes the formation of high Ni valency (γ-NiOOH with Raman feature at 477 and 557 cm^{-1}), improving the conductivity of Ni^{2+} by incorporating of mixed valence (Adler and Feinleib, 1970) to lower the system energy consumption. In summary, the element synergetic effect plays a crucial role in the catalytic property to split water. Our work has not only resulted in rejuvenating a well-known catalyst system into markedly higher catalytic efficient but also added some detailed surface information involving active phases transformation, which would stimulate further design of efficient NiFe-based compounds for commercial water electrolysis.
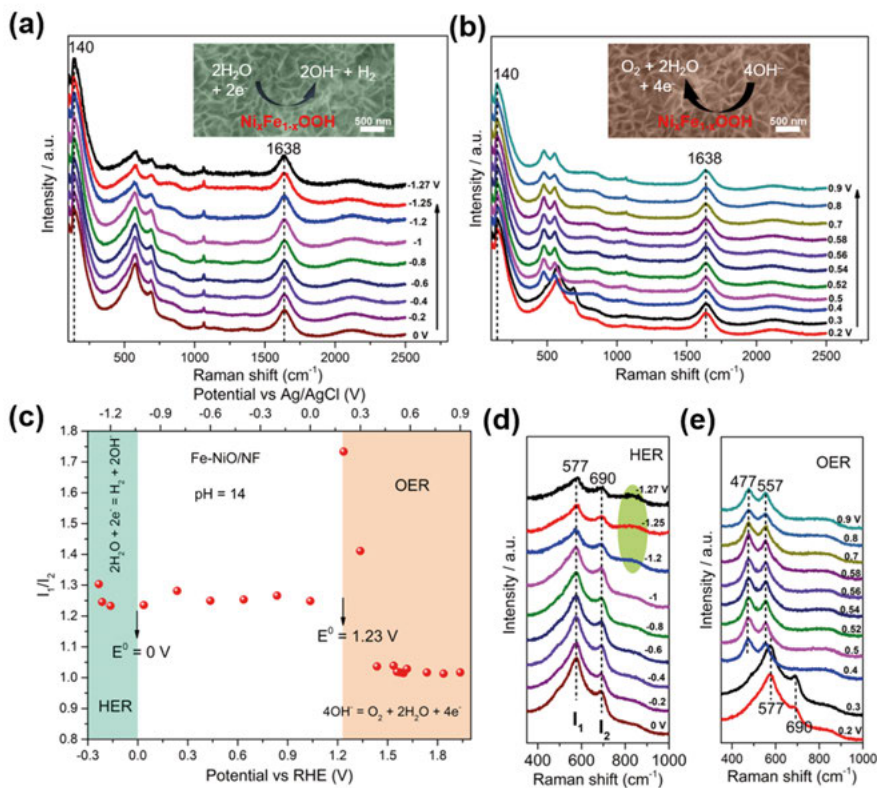
Figure 3.11 In-situ Raman spectra collected for Fe-NiO/NF at different potential ranges of (a) -1.27 V–0 V and (b) 0.2–0.9 V in 1 M NaOH. All applied potentials are vs Ag/AgCl (3 M KCl). (c) The intensity ratio of the two main peaks (I_1 to I_2) in the Raman spectra as a function of potentials. (d) and (e) are the magnification of (a) and (b), respectively.

3.1.3 NiFe LDH as an efficient bifunctional electrocatalyst

Figure 3.12 shows an illustration of the fabrication pathway of NiFe LDH by the hydrothermal method on Ni foam. As reported (Long et al., 2014; Lu et al., 2014), we also found that NiFe LDH is a promising electrocatalyst for OER in alkaline water splitting. Interesting, the NiFe LDH initial material in our work can be dynamically self-optimized into an efficient HER catalyst during 100 h aging process in 1 M N_2-saturated KOH. As shown in Figure 3.13a, the current density exhibits a remarkable increase from 9.3 mA cm^{-2} to 12.7 mA cm^{-2} in a two-electrode configuration. Figure 3.13b compared the catalytic property of initial and aged NiFe LDH for overall water splitting by LSV, which shows that the aged catalyst is significantly improved. The aged, or activated, catalyst requires only 1.48 V and 1.29 V to achieve a current density of 10 mA cm^{-2} and 1 mA cm^{-2} in a two-electrode cell, corresponding to electricity-to-hydrogen efficiencies of 83%-95%, compared to the lower

heating value of hydrogen (237.18 kJ per mol produced H_2 or 1.229 V). This is much higher than current commercial electrolyzers that operate at an efficiency between 60 to 73% (Turner, 2004), although usually at a higher current density. From the half-reaction (Figure 3.13c and d), we found that the dominant contribution for this quite remarkable activity improvement of water splitting is due to the aged HER catalysts. As shown in Figure 3.13e, the improved catalytic performance of aged NiFe LDH is plotted together with the other catalysts measured under the same condition. Overall, the aged NiFe-LDH requires only 243 mV overpotential for the full water splitting at 10 mA cm^{-2}, which is significantly less than that of commercial Pt foil with a total overpotential of 494 mV.
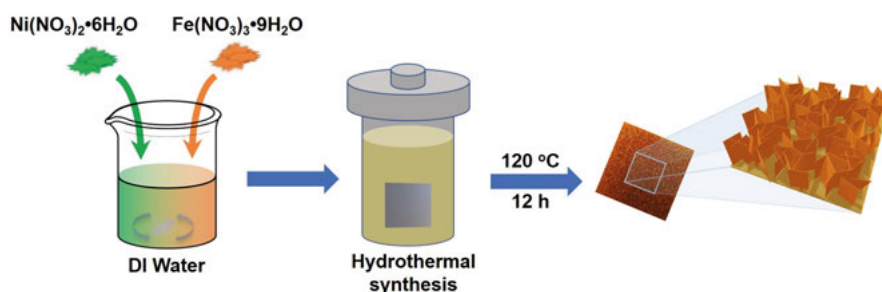
Figure 3.12 Illustration of the preparation of NiFe LDH NSs on Ni foam.
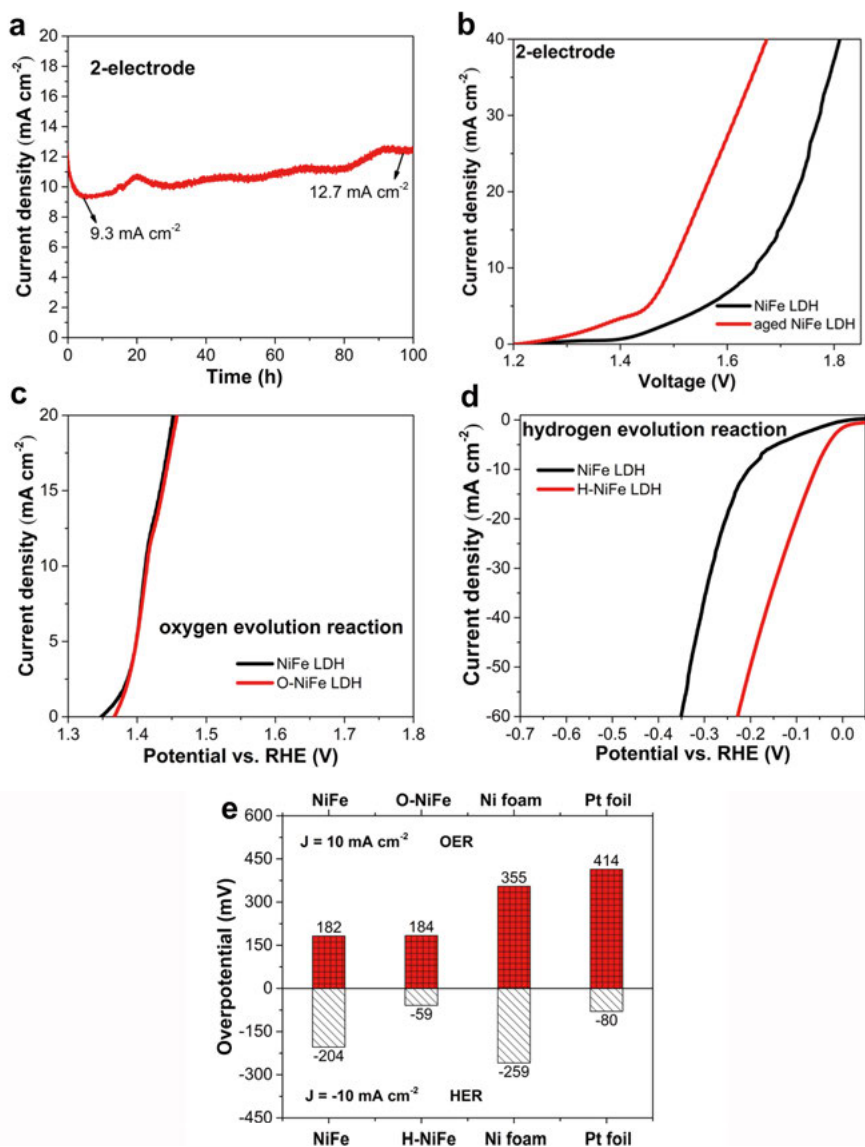
Figure 3.13 (a) J-t curve of NiFe LDH in a two-electrode system at an applied potential of 1.7 V, (b) LSV curves of initial NiFe LDH (NiFe LDH//NiFe LDH) and aged NiFe LDH (O-NiFe LDH//H-NiFe LDH) as a bifunctional catalyst in 1 M KOH for overall water electrolysis in a two-electrode system, (c) OER and (d) HER LSV curves of initial NiFe LDH and aged NiFe LDH with a sweep rate of 5 mV s⁻¹ in a three-electrode system, (e) overpotentials obtained from OER and HER LSV curves at the current density of 10 mA cm⁻² without iR compensation in 1 M KOH.

The multi-step chronopotentiometric curves in Figure 3.14a further confirms that the catalytic improvement is mainly ascribed to the aged NiFe LDH for HER (H-NiFe LDH). The electrochemical active surface area is a vital factor

58

for the catalytic performance, which can be estimated by C_{dl} by CV measured in the non-faradic range (Lukowski et al., 2013). As shown in Figure 3.14b, the C_{dl} of H-NiFe LDH (7.22 mF cm^{-2}) is approximately three times larger than that of NiFe LDH (2.16 mF cm^{-2}), leading to more exchangeable ions between catalytic active sites and the electrolyte and thus increase the electrolysis yield. In addition, the Tafel slope is typically used to evaluate reaction kinetics, reflecting the influence of overpotential on the steady-state current density. From Figure 3.14c, it is clear that the Tafel slope of H-NiFe LDH is 62.3 mV dec^{-1}, lower than that of NiFe LDH (78.39 mV dec^{-1}). The smaller Tafel slope shows the favorable catalytic property of H-NiFe LDH for HER process. Moreover, the measured Tafel slopes for both NiFe-LDH and H-NiFe LDH are between the theoretical rate-determining value (Shinagawa et al., 2015) of Volmer (120 mV dec^{-1}) and Heyrovsky (40 mV dec^{-1}), suggesting that their HER processes proceed *via* Volmer-Heyrovsky steps. Based on the Tafel equation *η=b×logJ+a*, the exchange current density (*J$_0$*) of NiFe LDH and H-NiFe LDH is estimated to be 0.38 mA cm^{-2} and 1.85 mA cm^{-2}, respectively. A larger *J$_0$* signifies that the material possesses a large surface area, fast electron transfer rate, and favorable HER kinetic (Wang et al., 2017), which represents that the H-NiFe LDH has obtained markedly improved HER activity *via* self-optimization. As seen in Figure 4.14d, the Tafel slope of O-NiFe LDH (28.83 mV dec^{-1}) is similar to that of NiFe LDH (34.34 mV dec^{-1}), close to *2.303(RT/2F)* V decade^{-1} at 298.15 K, indicating that the combination of MOH is rate determining (Bockris, 1956; Shinagawa et al., 2015).
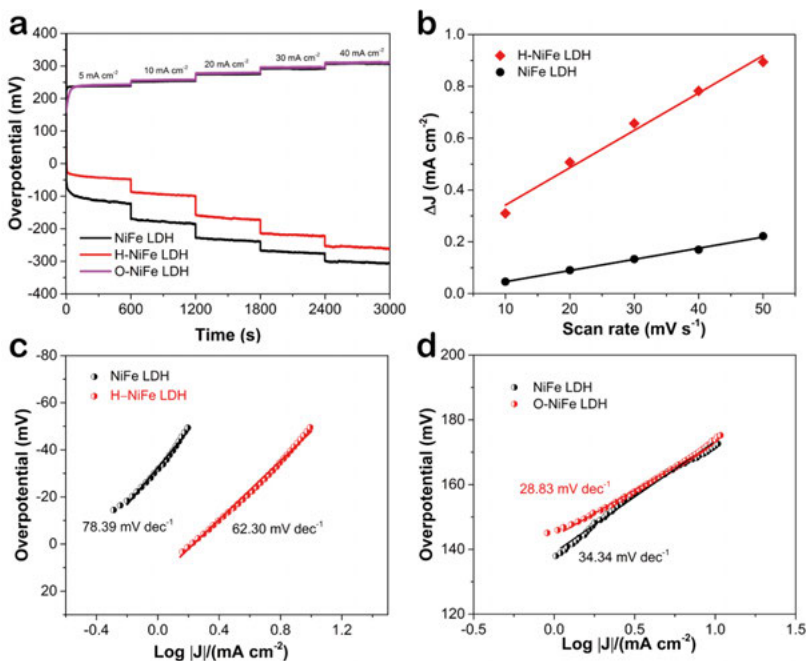
Figure 3.14 (a) Multistep chronopotentiometric test at different current densities of 5 mA cm⁻², 10 mA cm⁻², 20 mA cm⁻², 30 mA cm⁻² and 40 mA cm⁻² based on the geometric surface area, without iR correction in 1 M KOH, (b) differences in charging current density (J_a-J_c) plotted against scan rates. The linear fitting slope is approximating twice of C_{dl}, which is used to represent the ECSA. Tafel plots of catalysts under (c) HER and (d) OER in 1 M KOH at a scan rate of 5 mV s⁻¹ with 100% iR compensation.

The local crystal structure was characterized by selected area electron diffraction (SAED) in Figure 3.15a, indicating that the initial and aged NiFe LDH have the same diffraction pattern, while the crystallinity of catalysts increased during the OER and HER processes. The dynamically enhanced crystallinity can highly promote the charge and ion transport and finally lead to improved catalytic performance. The composition and element valence state of initial and aged catalysts were obtained by XPS (Figure 3.15 b and c). There is a slight increase in Ni^{3+} with respect to Ni^{2+} for O-NiFe LDH and a more pronounced increased in the valence of H-NiFe LDH; the spectrum peak of O 1s is also changing; i.e., the species after alkaline OER and HER are different. As these valance changes are measured *ex-situ*, they cannot be assigned to the active state during an applied potential or be certified to be from the active state or depleted state. To characterize the dynamic interfacial phases of the anode and cathode at applied potentials in the electrolyte, *in-situ* Raman spectroscopy was utilized as a function of potentials.
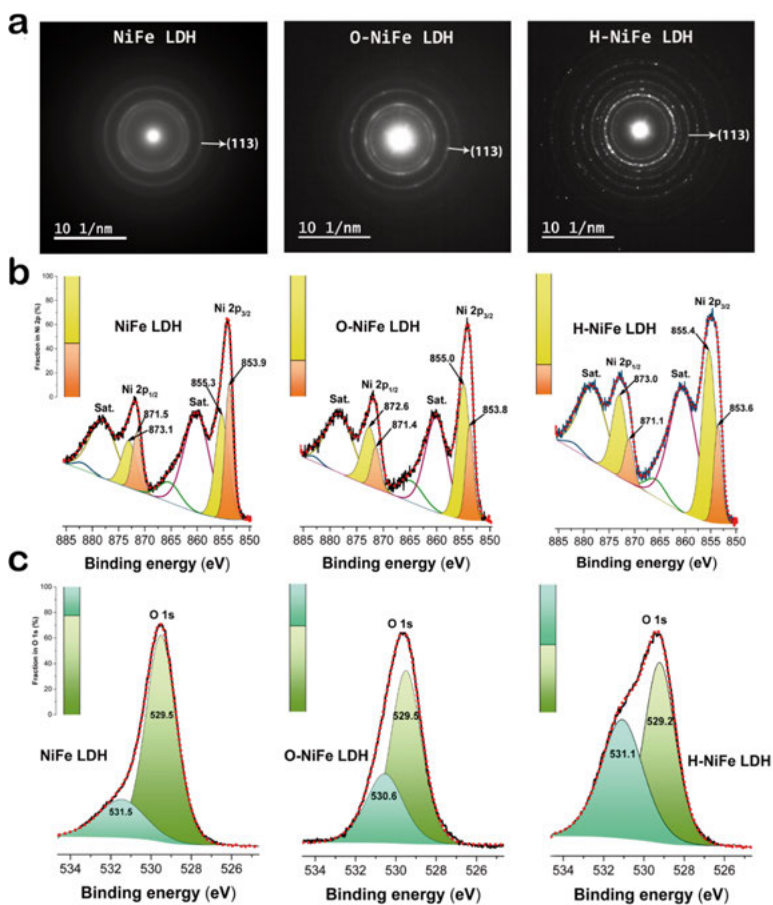
Figure 3.15 (a) SAED of initial and aged NiFe LDH, (b) Ni 2p and (c) O 1s XPS spectrum of NiFe LDH, H-NiFe LDH, and O-NiFe LDH. The color columns present the peak area integration ratio.

Figure 3.16 and 3.17 show the transformation of interfacial active phases with increased overpotential for OER and HER on the surface of NiFe LDH, respectively. The observed Raman bands of 477 ± 1 and 557 ± 1 cm^{-1} under OER process are consistent with spectral features of γ-NiOOH where the average oxidation state of Ni is +3.3 to 3.7 (Klaus et al., 2015; Yeo and Bell, 2012), while the Raman feature at 455 and 526 cm^{-1} under the HER process match well with metal-oxygen vibrations of Ni(OH)$_2$ (Hall, 2014) and FeOOH (Fe^{3+}) (Hanesch, 2009). Moreover, two broad vibration features turn up at around 840 cm^{-1} and 1600 to 2000 cm^{-1} (violet circles) after the overpotential of –150 mV, which can be assigned to hydrated nickel (Krasser and Renouprez, 1979; Nicol, 1992; Stockmeyer et al., 1980). These results show reliable evidence that Ni and Fe sites contribute differently to the catalytic activity under the interference of external voltage. In short, their synergistic effect is conducive

to the progress of both HER and OER, resulting in the excellent catalytic performance of NiFe-based oxide as a bi-functional electrocatalyst.

Based on previous research (Conway and Tilak, 1992; Subbaraman et al., 2012) and the analysis of our results, the reaction processes on NiFe LDH undergo as Eqn. 3.2–3.4 for OER and Eqn. 3.5–3.6 for HER.

OER process:

$$MO + OH^- \rightarrow OH_{ads}{-}MO + e^- \tag{3.2}$$

$$OH_{ads}{-}MO + OH^- \rightarrow O{-}MO + H_2O + e^- \tag{3.3}$$

$$2O{-}MO \rightarrow 2MO + O_2 \tag{3.4}$$

HER process:

$$H_2O + NiO + e^- \leftrightarrow H_{ads}{-}NiO + OH^- \tag{3.5}$$

$$H_2O + H_{ads}{-}NiO + e^- \leftrightarrow NiO + H_2 + OH^- \tag{3.6}$$
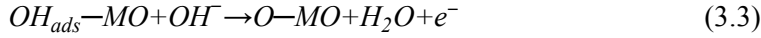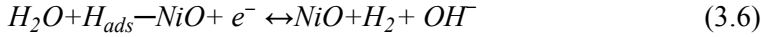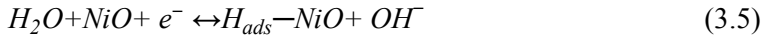
where M denotes Fe active sites at low overpotentials ($\eta < 200$ mV), while it represents Ni active sites at modest overpotentials ($\eta \sim 200$–300 mV).
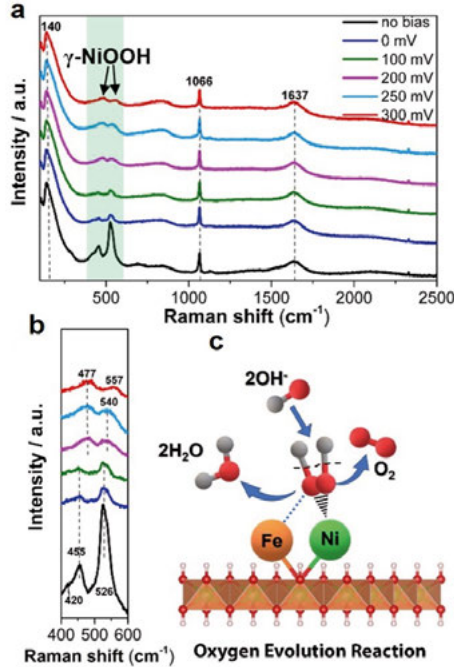
Figure 3.16 (a) In-situ Raman spectra with a large wavenumber region measured on NiFe LDH at various overpotentials vs RHE for OER in 1 M KOH, (b) magnification of the green region in (a), (c) schematic illustration of the derived OER mechanism on NiFe LDH.
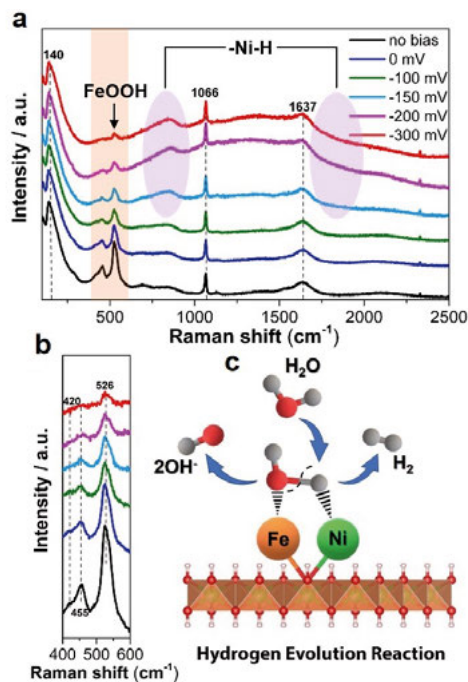
Figure 3.17 (a) In-situ Raman spectra with a large wavenumber region measured on NiFe LDH at various overpotentials vs RHE for HER in 1 M KOH, (b) magnification of the orange region in (a), (c) schematic illustration of the derived HER mechanism on NiFe LDH.

3.2 Cu-based mixed metal oxide for CO_2 reduction

This part of the work investigates the formation of $CuInO_2$ nanoparticles based on pre-catalyst Cu_2O thin film onto an ITO interlayer, eventually leading to a remarkably higher performance of CO_2 reduction. Cu_2O thin film and ITO interlayer were prepared according to the detailed procedure described in section 2.1.4. As seen in Figure 3.18a, both Cu_2O/ITO/FTO and Cu_2O/FTO show an electrocatalytic activity for CO_2 reduction, while Cu_2O/ITO/FTO exhibits a much lower onset overpotential and approximately three times better catalytic activity than that of Cu_2O/FTO. Figure 3.18b and c show the current density response with various applied potentials tested in CO_2-saturated acetonitrile with 0.1 M Bu_4NPF_6. It is evident that the catalytic performance has been significantly improved in the presence of an ITO layer. As the applied potential rises, the catalytic activity of Cu_2O/ITO/FTO also shows a notable increase in comparison with that of Cu_2O/FTO.
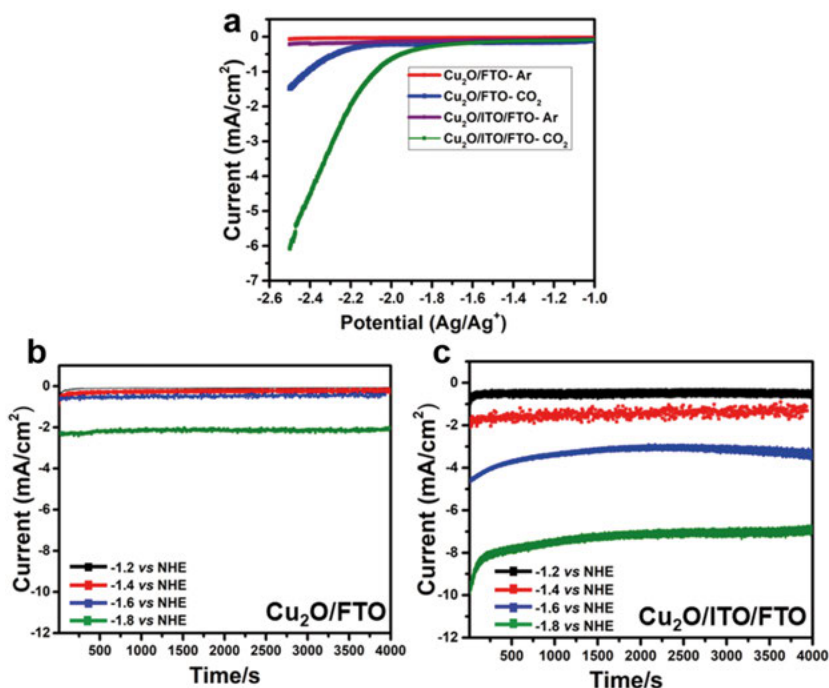
Figure 3.18 LSV curves of Cu_2O/FTO and Cu_2O/ITO/FTO for CO_2 reduction at a scan rate of 50 mV/s in 0.1 M Bu_4NPF_6 in Acetonitrile, the current density response as a function of different applied potentials of (b) Cu_2O/FTO electrode and (c) Cu_2O/ITO/FTO electrode.

In order to find out the real active catalyst for CO_2 reduction, we applied *in-situ* Raman spectroscopy at a constant applied potential of –1.8 V *vs* NHE. The spectral features revealed a conversion of Cu_2O to delafossite $CuInO_2$ as shown in Figure 3.19. The band at 102, 135, 214, 378 cm^{-1} are attributable to Cu_2O (Meyer et al., 2012) before starting the catalytic reaction. As the reaction proceeds on the electrode of Cu_2O/FTO, all Raman bands gradually attenuated over time. However, the change observed on Cu_2O/ITO/FTO electrode was significantly different from that seen on Cu_2O/FTO electrode. In addition to the different attenuation rate of the Raman feature at 102 and 135 cm^{-1}, the most prominent finding observed on Cu_2O/ITO/FTO is the appearance of two new Raman bands at 468 cm^{-1} and 562 cm^{-1} after 1 h CO_2 reduction, which can be assigned to delafossite $CuInO_2$ (Mazumder et al., 2013; Pellicer-Porres et al., 2006). This was further supported by linear response density functional theory (DFT) calculations as shown in Figure 3.20. The new Raman features reveal the creation of a new phase in the conversion process from the precursor phases to the real active CO_2 reduction catalysts with dramatically enhanced catalytic performance.
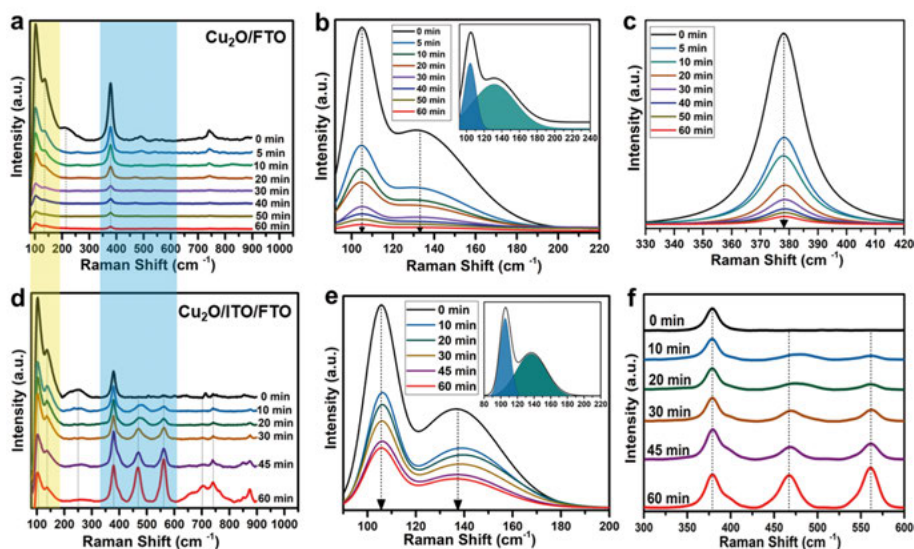
Figure 3.19 In-situ Raman spectra collected in acetonitrile with 0.1 M Bu₄NPF₆ at a potential of −1.8 V vs NHE as a function of the reaction time for (a) Cu₂O/FTO electrode, and (d) Cu₂O/ITO/FTO, (b, c) magnification of different wavenumber regions of a, (e, f) the magnification of different wavenumber regions of d.
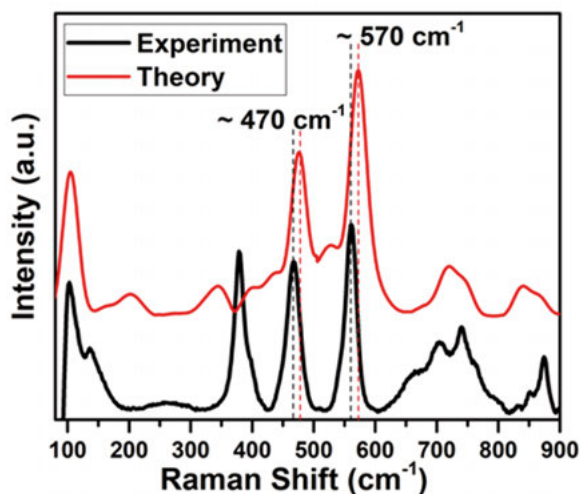

Figure 3.20 The comparison of DFT calculated Raman spectrum of the CuInO₂ (012) surface and experimental Raman spectrum of as-obtained material after 1 h CO₂ reduction at a potential of −1.8 V vs NHE.

The surface morphology and elemental dispersion were investigated by SEM and EDS as shown in Figure 3.21. Figure 3.21a and b show the changes in surface morphology of as-prepared Cu₂O thin film from polyhedral shapes to spheres. Besides copper and oxygen, indium and tin are also observed in the elemental mapping results as shown in Figure 3.21c-g. Given these results, a

plausible mechanism is that the released copper cations react with the ITO layer to form a new mixed metal oxide nanoparticles $CuInO_2$, which is investigated in more detail in **Paper V**. The presence and crystallinity of $CuInO_2$ structure were further verified by the XRD pattern in Figure 3.22. The XRD pattern of Cu_2O/FTO measured before and after the catalytic reaction (Figure 3.22a-c) indicate that the composition of Cu_2O crystalline was decreasing, while the diffraction peak of Cu (111) (ICDD: 01-070-3039) (Eugénio et al., 2014) increased after the CO_2 reduction. In addition, as shown in Figure 3.22d-f, the diffraction peaks of Cu_2O and ITO decreased after the one-hour reaction. It is noteworthy that crystalline Cu metal was not detected, however, the diffraction peak of the delafossite $CuInO_2$ (012) was seen. Based on the results from electrochemical measurements, *in-situ* Raman spectrum, and material characterizations, we found that the formation of $CuInO_2$ greatly boosts the catalytic performance of CO_2 reduction.

In summary, this work reveals a conversion process from pre-catalyst Cu_2O and ITO layer to an active phase of $CuInO_2$ for CO_2 reduction. The creation and improved catalytic performance of this mixed metal oxide can possibly provide the inspiration and initial guidelines to design more efficient and robust catalysts for CO_2 reduction based on further Cu-based metal oxides or other intermetallic catalyst designs.
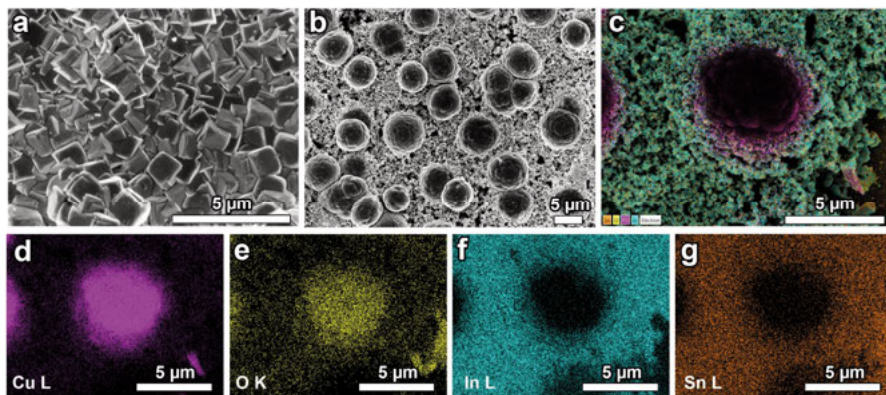
Figure 3.21 SEM images of Cu_2O/ITO/FTO before (a) and after (b) 1 h electrochemical measurement at −1.8 V vs NHE, (c) combined element mapping image, (d-g) element mapping of Cu, O, In and Sn.
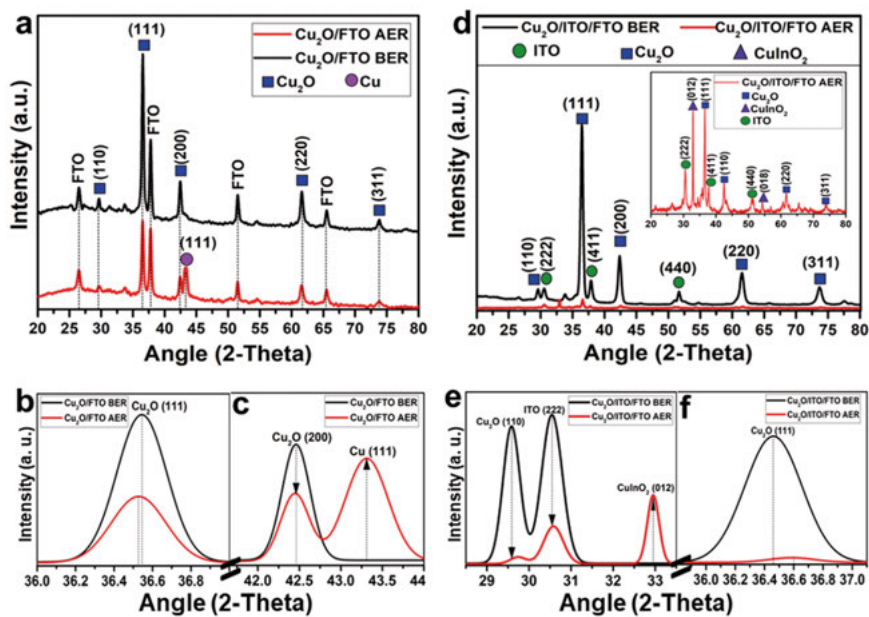
Figure 3.22 XRD patterns of Cu$_2$O/FTO (a-c) and Cu$_2$O/ITO/FTO (d-f) before and after one-hour CO$_2$ reduction at a potential of −1.8 V vs NHE.

4. Summary and conclusions

Efficient and cost-effective electrocatalysts are essential components of catalysis technology. In this thesis, we focus on developing efficient, cost-effective and stable transition metal-based electrocatalysts for alkaline water splitting and CO_2 reduction and understanding their catalytic reaction processes. The results can be summarized in three aspects.

Synthesis and characterization of different materials

NiO NFs were synthesized by a hydrothermal method in **Paper I**, where the pH value of synthetic precursor system was tuned to adjust both the crystal growth orientation and crystallization of $Ni(OH)_2$ NFs and eventually the resulting NiO NFs. With pH varied from 9 to 12, the structures of the NiO NFs were self-assembled from individual pieces into flower-like hierarchical hollow architectures because of the different conditions during synthesis. It was found that the pH value near to point of zero charge of $NiO/Ni(OH)_2$ system has an important influence on the crystal growth direction and self-assembled process, which can be utilized to control the resulting NiO nanostructures. The NiO NFs are active as OER catalysts in alkaline media and their activity is affected by the polycrystalline growth and morphology. The work shows that NiO NFs synthesized at pH 10 exhibits the lowest overpotential of 350 mV at 10 mA cm^{-2} compared with the other NFs. In **Paper II and III**, Fe-NiO NSs on Ni foam were prepared by a facile CBD method. The Raman shifts and XRD peaks indicate substitutional Fe doping into the cubic NiO nanostructure. The electrochemical characterization showed that the incorporation of Fe into NiO NSs improved the catalytic activity of both the OER and HER, even though the electrochemical surface area is relatively small. Combined with the results in **Paper I**, we assume that increasing the surface area of Fe-NiO NSs enables to improve the catalytic performance to a larger extent. NiFe LDH NSs on Ni foam were synthesized by a hydrothermal method in **Paper IV**, and further optimized by an aging process in 1 M KOH aqueous solution, which is denoted as H-NiFe LDH and O-NiFe LDH corresponding to HER and OER aging. The results revealed increased crystallinity and larger electrochemical active area with a significantly enhanced HER performance with 145 mV lower overpotential at 10 mA cm^{-2}. For electrocatalytic CO_2 reduction, the pre-electrocatalyst Cu_2O thin film in **Paper V** was prepared by electrochemical deposition at the galvanostatic mode with a constant current density of -0.16 mA cm^{-2} for 150 min in a two-electrode system, where a Pt mesh was

used as a counter electrode. The active catalyst $CuInO_2$ was dynamically formed during electrocatalytic CO_2 reduction at -1.8 V *vs* NHE and exhibited a remarkable catalytic improvement with a significantly lower overpotential requirement.
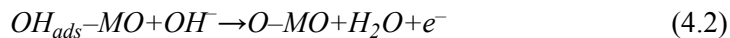
Identification of active species on the catalyst surface

In-situ Raman spectroscopy was utilized to probe the interfacial phases created during reactions in this thesis. The results in **Paper II** and **Paper IV** show that the active surface phases are different from the initial phases for alkaline water splitting. It is notable that the main function of Ni and Fe sites in both Fe-NiO NSs and NiFe LDH NSs during water electrocatalysis is altered with different applied potentials. As observed, the active species for HER are FeOOH and H_{ad}–$Ni^{\delta+}$ with a more obvious Raman feature at 750–950 cm^{-1} at the larger HER overpotential, whereas the active phase is γ-NiOOH for OER, showing a Raman band at around 477 and 557 cm^{-1}. These results suggest that the active species in NiFe (hydr)oxide are oxyhydroxides for alkaline water splitting. **Paper V** addressed the dynamic formation of active phase $CuInO_2$ under a vigorous catalytic CO_2 reduction on pre-catalyst Cu_2O thin film with ITO interlayer by experimental and theoretical Raman spectrum. Both of them verify the dynamic reconstruction by observing the appearance of two new predominant bands at 468 cm^{-1} and 562 cm^{-1} and two weaker scatterings at 720 cm^{-1} and 870 cm^{-1}.

Insight of reaction mechanism

In **Paper III** and **Paper IV**, we adopted impedance spectroscopy and Tafel plot analysis to investigate their reaction mechanism for both OER and HER. A negative loop was observed at low-frequency range for Fe-NiO and NiFe LDH for hydrogen generation. The results imply that the HER mechanism for Fe-NiO and NiFe LDH proceeds *via* by Volmer–Heyrovsky steps because the Volmer–Tafel reaction cannot lead to inductive behavior and is further confirmed by Tafel slope analysis. The OER mechanisms of Fe-NiO and NiFe LDH were analyzed from Tafel slope analysis as well. Even though the Tafel slopes of Fe-NiO NSs and NiFe LDH are different, they reveal the same rate-determining step followed by electrochemical oxide path if their different range for the Tafel plotting is considered. Combed with *in-situ* Raman spectroscopy, we infer that the OER and HER proceed as follows. M represents Fe active sites at low overpotentials ($\eta < 200$ mV), while, at modest overpotentials, it represents Ni active sites ($\eta \sim 200\text{-}300$ mV).

OER process:

$$MO+OH^-\rightarrow OH_{ads}\text{–}MO+e^- \tag{4.1}$$

$$OH_{ads}\text{–}MO+OH^-\rightarrow O\text{–}MO+H_2O+e^- \tag{4.2}$$

$$2O\text{–}MO\rightarrow 2MO+O_2 \tag{4.3}$$

HER process:

$$H_2O + NiO + e^- \leftrightarrow H_{ads} - NiO + OH^- \qquad (4.4)$$

$$H_2O + H_{ads} - NiO + e^- \leftrightarrow NiO + H_2 + OH^- \qquad (4.5)$$
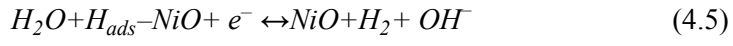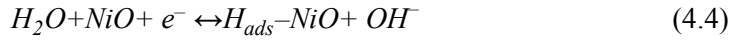
5. Ongoing studies and perspectives

Our general aim is to investigate and develop efficient, low-cost and robust electrocatalysts for energy conversion from water or CO_2 to chemical fuels. In addition to the study of Fe substitution of Ni in NiO, we also investigated the function of S substitution of O in NiO for alkaline water splitting. As shown in Figure 5.1, the catalytic performance is remarkably improved for both OER and HER in alkaline water splitting after the S substitution. Except for the catalytic improvement for oxygen evolution, Ni_3S_2 shows a strong self-oxidation around 1.48 V *vs* RHE (Figure 5.1a). In addition, after 5000 cycles, Ni_3S_2 has no significant degradation for HER (Figure 5.1b).
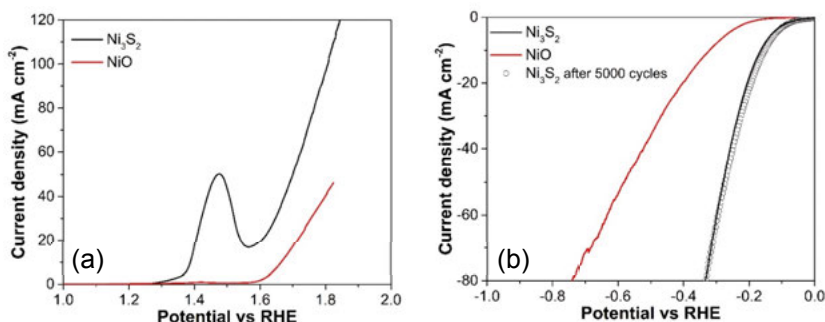
Figure 5.1 A representative LSV curves of (a) OER and (b) HER on NiO and Ni_3S_2 at 5 mV s^{-1} in 1 M KOH.

Then, the question is what occurs under the electrocatalytic reaction and what results in the catalytic improvement. From the view of solid-state chemistry, it is well known that the thermodynamic stability of metal sulfides is worse than that of metal oxides under oxidizing potentials (Jin, 2017). Moreover, in an aqueous electrochemical system, the stable thermodynamic metal state is alterable with the applied potential even at a constant pH, which is known as a Pourbaix diagram invented by Marcel Pourbaix. Figure 5.2 exhibits Ni Pourbaix diagrams on the basis of DFT and experimental (Expt) thermodynamic energies. To rational design of efficient and robust electrocatalysts, it is crucial to figure out interfacial reactions, including active species, active sites, elemental composition before and after reactions, etc. *In-situ* characterizations are necessary to uncover the dynamic process, such as *in-situ* Raman spectroscopy we used in this thesis, *in operando* X-ray absorption. On the other hand, electrodes show a high current density because of their oxidization.

Even though the electrochemical current density has been widely used to evaluate the catalytic performance of materials, the amount of gas generation is needed to be another visual standard for the catalytic activity of electrodes.
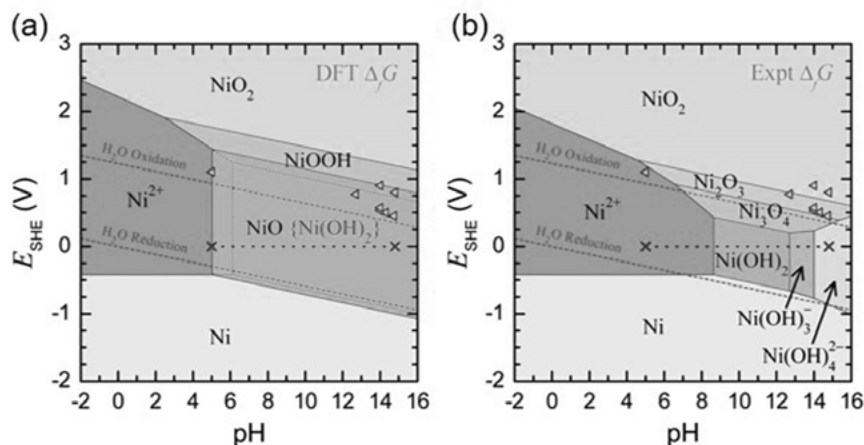

Figure 5.2 Electrode potential–pH (Pourbaix) diagrams of Ni ([Ni^{2+}] =10^{-6} mol/L, 298.15 K, 1.0 bar). © Reprinted permission from (Huang et al., 2017) Copyright 2017 American Chemical Society.

To realize the renewable energy conversion, one promising option is combining photovoltaic (PV)-technology and earth-abundant electrocatalysts into modular or integrated PV-EC device. In our project, the practical photovoltaic–water electrolysis (PV-WE) device was integrated tandem CIGS solar cell with our prepared electrocatalysts. The predicted operating current density of the combined PV-WE system is defined as the intersection of the measured J-V curves of tandem CIGS solar cell and as-prepared electrodes. Figure 5.3a shows the best as-measured current value of 9.1 mA cm^{-2}, which is corresponding to a solar-to-hydrogen efficiency (SHE) of 11.19%. The SHE of the integrated system under chopped illumination is 10.57% (Figure 5.3b), which is similar to the predicted value. The small loss may be from the external wire connection and the surface recombination. The result confirms the preliminary high activity of our system, even though the efficiency of our device needs to be improved more. As we discussed in chapter 3.1, NiFe LDH is more efficient than Fe-NiO for alkaline water splitting. Using NiFe LDH as electrodes would be the next step to develop the system efficiency of our PV–EC device.
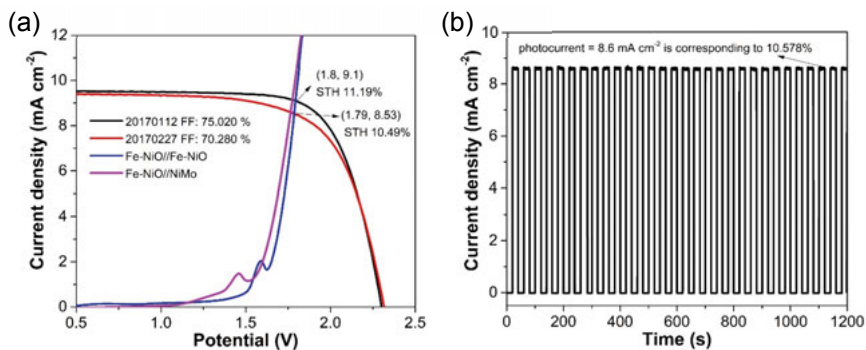
Figure 5.3 (a) J-V curves of CIGS tandem solar cell under AM 1.5 G 100 mW cm^{-2} illumination and as-prepared catalysts in a two-electrode system in 1 M NaOH. The illuminated surface area of CIGS solar cell is 2.4 cm^2 and the exposed area of catalysts is 1 cm^2. (b) J-t curve of the integrated PV-EC device without external bias under chopped with AM 1.5 G 100 mW cm^{-2} illumination.

6. Swedish summary (Svensk sammanfattning)

Det moderna samhället är i stort beroende av energi och för närvarande levereras den globala energin huvudsakligen av traditionella fossila bränslen, t.ex. olja, naturgas och kol. Fossila bränslen är dock inte förnybara och ger ett nettoutsläpp av koldioxid i atmosfären, vilket redan anses ge synliga förändringar av världens klimat. Sol- och vindenergi betraktas här som miljövänliga och förnybara energikällor och deras förmåga att möta framtida globala energibehov är väl dokumenterad. En av deras utmaningar inför storskalig användning är deras varierande energi-generering med varierande sol- och vindförhållanden under olika dygns- eller årstidsvariationer. Med tanke på de intermittenta förändringarna av atmosfäriska förhållanden är utvecklingen av effektiv lagringsteknik viktig för att möjliggöra tillväxt av förnybar el från sol- och vindenergi mot en lösning där de kan vara den primära energiförsörjningen. Ett tillvägagångssätt är att utveckla elektrokemisk teknik som möjliggör effektiv omvandling av vatten eller koldioxid till kemiska bränslen (vätgas eller kolväten) från förnybar elektricitet. Man kan sedan använda dessa bränslen vid behov där restprodukten endast är vatten vid förbränning av vätgas eller generering av elektricitet i en vätgas-bränslecell. Generering av kolväten från koldioxid kan ge alternativa sätt att ta hand om utsläpp från fabriker och minska den totala koldioxidemissionen, men kanske även kan byggas in i ett cykliskt system utan nettoutsläpp av växthusgas. Omvandling av intermittenta energikällor till kemiska bränslen med nollnätutsläpp skulle på så sätt kunna möjliggöra en hållbar energiförsörjning utan någon förändring i atmosfärsförhållandena. En fullständig realisering av effektiv el-till-bränsleomvandling är dock fortfarande begränsad av de stora överpotentialer som krävs för att göra detta med hög produktionshastighet och också användandet av element from platinagruppen som inte finns rikligt nog i jordskorpan för storskalig användning.

Denna avhandling ägnas åt utveckling och förståelse av elektrokatalysatorer baserade på vanliga övergångsmetaller och deras oxider, hydroxider och oxyhydroxider med de önskade egenskaperna att effektivt sönderdela vatten i vätgas (H_2) och syrgas (O_2) samt att reducera koldioxid (CO_2) med hög konverteringseffektivitet. Materialen tillverkas till små dimensioner (nanometerskala) för att optimera och kontrollera ytan som är aktiv för den katalytiska processen. I anslutning till detta måste grundläggande undersökningar av de processer som uppträder vid ytan också göras, eftersom de aktiva katalysatormaterialen vid ytan under katalysen ofta inte är samma som utgångsmaterialen

och kan också dynamiskt omformas eller brytas ned under de krävande för-hållandena under själva katalysen. Katalysprocesserna som förekommer på ytan i detta arbete karakteriserat under själva reaktionen i elektrolyten genom att skicka in laserljus på materialen och analysera små förändringar i våglängden på ljuset som kommer tillbaka. Tekniken kallas Ramanspektroskopi ut-nyttjar att vibrationer i molekyler och material kan ta upp en del av ljuset som motsvarar vibrationerna i bindningarna i materialet, förutsatt att elektronden-siteten som bidrar till bindningen kan ändra sin förmåga att polariseras under vibrationen. En stor fördel med Ramanspektroskopin är att den kan analysera vilka material som finns på katalysatorytan och hur de förändras under olika reaktionsbetingelser.

I första delen av avhandlingen beskrivs bakgrundsteorin för elektrolys av vatten, koldioxidsreduktion och en kort genomgång av experimentellt tillvä-gagångssätt för att tillverka nano-katalysatorerna och karakteriseringstekni-kerna. Arbetet med att utveckla och undersöka tre olika men besläktade elektrokatalysatorsystem beskrivs sedan. Katalysatormaterialen är avsedda för högpresterande elektrokatalys av vatten och är NiO nanoflak formade i tunna ytstrukturer, Fe-dopade NiO-nanoskikt och självoptimerade NiFe-skiktade dubbelhydroxider. De självaggregerande nanoflaken av NiO visar drastiskt olika prestanda för syreutvecklingsreaktionen (OER) där ett tillvägagångssätt och styrning av detta presenteras (**Artikel I**) och illustreras i Figur 6.1.
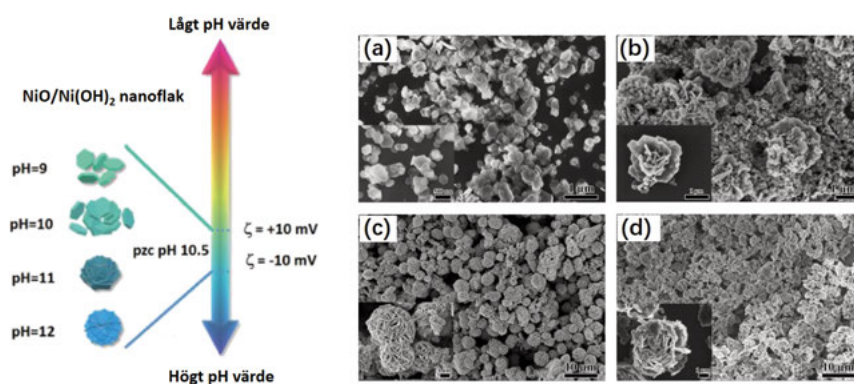
*Figur 6.1 (Vänster) Illustration av hur ytladdningen runt den oladdade ytan (point-of-zero-charge, PZC) beror av pH och kan användas för att syra kristalltillväxt och aggregering. a)-d) visar nanokatalysatorsystemet vid tillverkning mellan pH=9 till pH=12. Skalstrecket är 1 μm i a) och b) och 10 μm i d) och e) och de infällda bilderna visar högre förstoring (bilderna hämtade från **Artikel I**.)*

Förutom den morfologiska effekten på den katalytiska egenskapen är närvaron av Fe också funktionell för att förbättra den katalytiska aktiviteten för både OER och väteutvecklingsreaktionen (HER) där in-situ Ramanspektroskopi

och elektrokemisk impedansspektroskopi (EIS) använd i **Artikel I** och **Artikel II** för att analysera ytfaser och reaktionsmekanismer. Ett katalysatorsystem baserat på skiktade NiFe-dubbelhydroxider (NiFe-LDH) utvecklades och studerades i **Artikel IV** och fungerade som en bi-funktionell katalysator, dvs var aktiv både för OER och HER. Den övergripande katalytiska prestandan hos NiFe LDH förbättras dramatiskt med en dynamisk självoptimering, speciellt för HER, där överpotentialen för vätgasreaktionen minskade från 206 mV till 59 mV vid 10 mA cm^{-2}. Den aktiverade katalysatorn krävde endast 1,48 V och 1,29 V för att uppnå en strömtäthet av 10 mA cm^{-2} och 1 mA cm^{-2} i en tvåelektrodcell, vilket motsvarar en omvandlingsverkningsgrad el-till-väte på 83%─95%, jämfört med det lägre värmevärdet av väte (237,18 kJ per mol producerad H_2 eller 1,229 V). För att få insikt i ytreaktionsprocesserna användes en rad olika tekniker, ex-situ XPS, TEM, EELS, *in situ* Ramanspektroskopi och EIS, för att karakterisera och förstå de dominerande oxidationstillstånden, kristalliniteten, de aktiva faserna och de dominerande reaktionsmekanismerna som sammanfattas i Figur 6.2.
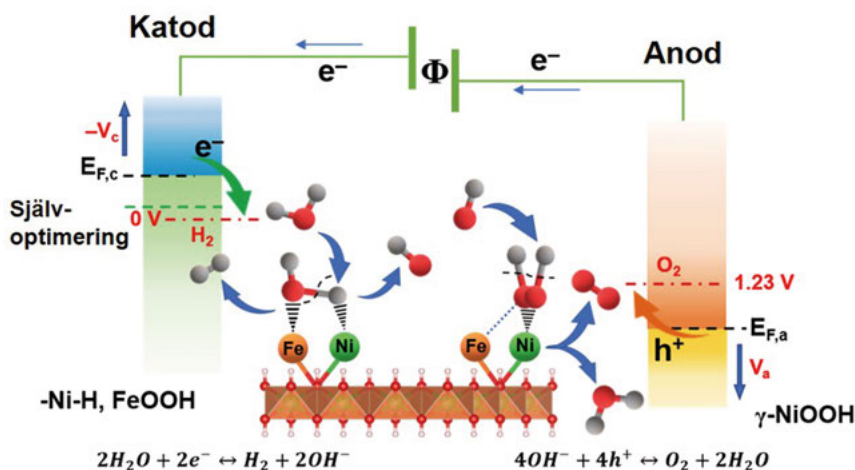
*Figur 6.2 Schematisk representation av den elektrokatalytiska processeerna för den bifunktionella NiFe-LDH-katalysatorn via oxyhydroxider. FeOOH och Ni$^{\delta+}$-H är de bildade ytfaserna under HER-processen, medan γ-NiOOH är den observerade fasen under OER-processen (från **Artikel IV**).*

I **Artikel V** demonstrerades att dynamiskt bildade CuInO$_2$ nanopartiklar bildar högpresterande elektrokatalysatorer för CO$_2$-reduktion med en låg överpotential. *In-situ* Raman-spektroskopi användes för att avslöja och förstå bildningen av CuInO$_2$ baserade på ett initialmaterial bestående av kopparoxid (Cu$_2$O) på ett lager av Indiumtennoxid (ITO) under den elektrokemiska reaktionen. Densitetsfunktionsteori (DFT) -beräkningar stödde de experimentella vibrationssignalerna tillsammans med röntgendiffraktionsstudier. Fynden ger

viktiga ledtrådar om hur Cu-baserade elektrokatalysatorer kan formas till mer aktiva katalysatormaterial och kan även ge inspiration för andra Cu-baserade intermetalliska oxider med hög effektivitet för CO_2-reduktion.

Acknowledgments

Finally, I would like to give a wholehearted thanks to my husband, Zhicheng. Thank you for being here with me. I really appreciate your patience and selfless dedication to our family. I hope I can understand the meaning of home better in the near future. Love you! I believe we will be different because of each other.

<div align="right">

Zhen Qiu
2019-03-28
Ångstrom Laboratory

</div>

References

Adler, D., and Feinleib, J. (1970). Electrical and optical properties of narrow-band materials. 2, 3112.

Anantharaj, S., Ede, S. R., Sakthikumar, K., Karthick, K., Mishra, S., and Kundu, S. (2016). Recent trends and perspectives in electrochemical water splitting with an emphasis on sulfide, selenide, and phosphide catalysts of Fe, Co, and Ni: a review. Acs Catalysis 6, 8069-8097.

Balat, M. (2008). Potential importance of hydrogen as a future solution to environmental and transportation problems. 33, 4013-4029.

Ball, M., and Weeda, M. (2015). The hydrogen economy–vision or reality? 40, 7903-7919.

Barber, J. (2009). Photosynthetic energy conversion: natural and artificial. 38, 185-196.

Barbir, F. (2005). PEM electrolysis for production of hydrogen from renewable energy sources. Solar energy 78, 661-669.

Basova, T. V., and Kolesov, B. A. (1998). Raman polarization studies of the orientation of molecular thin films. Thin Solid Films 325, 140-144.

Benson, E. E., Kubiak, C. P., Sathrum, A. J., and Smieja, J. M. (2009). Electrocatalytic and homogeneous approaches to conversion of CO_2 to liquid fuels. Chemical Society Reviews, 38(1), 89-99.

Birla Singh, M., and Kant, R. (2014). Theory of anomalous dynamics of electric double layer at heterogeneous and rough electrodes. The Journal of Physical Chemistry C 118, 5122-5133.

Birman, J. L., Cummins, H. Z., and Rebane, K. K. (1979). Light Scattering in Solids (Springer).

Bockris, J.O.M. (1956). Kinetics of activation controlled consecutive electrochemical reactions: anodic evolution of oxygen. The Journal of Chemical Physics 24, 817-827.

Bourikas, K., Kordulis, C., Lycourghiotis, A., (2005). Differential potentiometric titration: development of a methodology for determining the point of zero charge of metal (hydr) oxides by one titration curve. Environmental science & technology, 39(11), 4100-4108.

Campion, A. (1985). Raman spectroscopy of molecules adsorbed on solid surfaces. Annual Review of Physical Chemistry 36, 549-572.

Cépas, O., Haerter, J., and Lhuillier, C. (2008). Detection of weak emergent broken-symmetries of the kagome antiferromagnet by Raman spectroscopy. Physical Review B 77, 172406.

Cheng, Y., and Jiang, S. P. (2015). Advances in electrocatalysts for oxygen evolution reaction of water electrolysis-from metal oxides to carbon nanotubes. Progress in natural science: materials international, 25(6), 545-553.

Conway, B., and Tilak, B. (1992). Behavior and characterization of kinetically involved chemisorbed intermediates in electrocatalysis of gas evolution reactions. In Advances in catalysis (Elsevier), pp. 1-147.

Cook, T.R., Dogutan, D.K., Reece, S.Y., Surendranath, Y., Teets, T.S., and Nocera, D.G. (2010). Solar energy supply and storage for the legacy and nonlegacy worlds. Chemical reviews 110, 6474-6502.

Costentin, C., Robert, M., & Savéant, J. M. (2013). Catalysis of the electrochemical reduction of carbon dioxide. Chemical Society Reviews, 42(6), 2423-2436.

Crabtree, G.W., Dresselhaus, M.S., and Buchanan, M.V. (2004). The hydrogen economy. Physics today, 57(12), 39-44.

Daniel, M.-C., and Astruc, D. (2004). Gold nanoparticles: assembly, supramolecular chemistry, quantum-size-related properties, and applications toward biology, catalysis, and nanotechnology. Chemical reviews 104, 293-346.

De Faria, D.L.A., Venâncio Silva, S., and De Oliveira, M.T. (1997). Raman microspectroscopy of some iron oxides and oxyhydroxides. 28, 873-878.

Diard, J.-P., LeGorrec, B., and Maximovitch, S. (1990). Etude de l'activation du degagement d'hydrogene sur electrode d'oxyde de nickel par spectroscopie d'impedance. 35, 1099-1108.

Dodds, P.E., and Demoullin, S. (2013). Conversion of the UK gas system to transport hydrogen. 38, 7189-7200.

Doyle, R.L., and Lyons, M.E. (2013). An electrochemical impedance study of the oxygen evolution reaction at hydrous iron oxide in base. 15, 5224-5237.

Dresselhaus, M.S., and Thomas, I.L. (2001). Alternative energy technologies. 414, 332.

Drüschler, M., Huber, B., Passerini, S., and Roling, B. (2010). Hysteresis effects in the potential-dependent double layer capacitance of room temperature ionic liquids at a polycrystalline platinum interface. The Journal of Physical Chemistry C 114, 3614-3617.

Eugénio, S., Silva, T.M., Carmezim, M.J., Duarte, R.G., and Montemor, M.F. (2014). Electrodeposition and characterization of nickel–copper metallic foams for application as electrodes for supercapacitors. 44, 455-465.

Ferraro, J.R. (2003). Introductory raman spectroscopy (Elsevier).

Fominykh, K., Chernev, P., Zaharieva, I., Sicklinger, J., Stefanic, G., Döblinger, M., Müller, A., Pokharel, A., Böcklein, S., Scheu, C., and Bein, T. (2015). Iron-doped nickel oxide nanocrystals as highly efficient electrocatalysts for alkaline water splitting. 9, 5180-5188.

Fujishima, A., and Honda, K. (1972). Electrochemical photolysis of water at a semiconductor electrode. nature 238, 37.

Glenk, G., and Reichelstein, S. (2019). Economics of converting renewable power to hydrogen. 1.

Graciani, J., Mudiyanselage, K., Xu, F., Baber, A. E., Evans, J., Senanayake, S. D., ... and Rodriguez, J. A. (2014). Highly active copper-ceria and copper-ceria-titania catalysts for methanol synthesis from CO_2. Science, 345(6196), 546-550.

Hall, D.S. (2014). An electrochemical and spectroscopic investigation of nickel electrodes in alkaline media for applications in electro-catalysis (Université d'Ottawa/University of Ottawa).

Hanesch, M. (2009). Raman spectroscopy of iron oxides and (oxy) hydroxides at low laser power and possible applications in environmental magnetic studies. 177, 941-948.

Harrington, D.A., and Conway, B.E. (1987). ac Impedance of Faradaic reactions involving electrosorbed intermediates–I. Kinetic theory. Electrochimica Acta 32, 1703-1712.

Hoegh-Guldberg, O., Jacob, D., Taylor, M., Bindi, M., Brown, S., Camilloni, I., Diedhiou, A., Djalante, R., Ebi, K., and Engelbrecht, F. (2018). Chapter 3: Impacts of 1.5 ºC global warming on natural and human systems (Intergovernmental Panel on Climate Change), pp. 1-243.

Holladay, J.D., Hu, J., King, D.L., and Wang, Y. (2009). An overview of hydrogen production technologies. Catalysis Today 139, 244-260.

Hori, Y.I. (2008). Electrochemical CO_2 reduction on metal electrodes. In Modern aspects of electrochemistry (pp. 89-189). Springer, New York, NY.

Huang, L.F., Hutchison, M.J., Santucci, R.J., Scully, J.R., and Rondinelli, J.M. (2017). Improved electrochemical phase diagrams from theory and experiment: the Ni–water system and its complex compounds. The Journal of Physical Chemistry C 121, 9782-9789.

International Energy Agency, 2018

Jain, S.M., Qiu, Z., Häggman, L., Mirmohades, M., Johansson, M.B., Edvinsson, T., and Boschloo, G. (2016). Frustrated Lewis pair-mediated recrystallization of $CH_3NH_3PbI_3$ for improved optoelectronic quality and high voltage planar perovskite solar cells. Energy & Environmental Science 9, 3770-3782.

Jin, S. (2017). Are metal chalcogenides, nitrides, and phosphides oxygen evolution catalysts or bifunctional catalysts? ACS Energy Letters 2, 1937-1938.

Joshi, U.S., Matsumoto, Y., Itaka, K., Sumiya, M., and Koinuma, H. (2006). Combinatorial synthesis of Li-doped NiO thin films and their transparent conducting properties. Applied Surface Science 252, 2524-2528.

Klaus, S., Cai, Y., Louie, M.W., Trotochaud, L., and Bell, A.T. (2015). Effects of Fe electrolyte impurities on $Ni(OH)_2$/NiOOH structure and oxygen evolution activity. The Journal of Physical Chemistry C 119, 7243-7254.

Ko, J.W., Kim, S.-W., Hong, J., Ryu, J., Kang, K., and Park, C.B. (2012). Synthesis of graphene-wrapped CuO hybrid materials by CO_2 mineralization. Green Chemistry 14, 2391-2394.

Kohli, R., and Mittal, K.L. (2011). Developments in surface contamination and cleaning, volume 4: Detection, characterization, and analysis of contaminants (William Andrew), pp.1-352.

Koopmans, T. (1934). Über die zuordnung von wellenfunktionen und eigenwerten zu den einzelnen elektronen eines atoms. Physica 1, 104-113.

Kosacki, I., Suzuki, T., Anderson, H.U., and Colomban, P. (2002). Raman scattering and lattice defects in nanocrystalline CeO_2 thin films. Solid State Ionics 149, 99-105.

Kosmulski, M. (2018). The pH dependent surface charging and points of zero charge. VII. Update. Advances in Colloid and Interface Science 251, 115-138.

Krasser, W., and Renouprez, A.J. (1979). Raman scattering of hydrogen chemisorbed on silica-supported nickel. Journal of Raman Spectroscopy 8, 92-94.

Kreuter, W., and Hofmann, H. (1998). Electrolysis: the important energy transformer in a world of sustainable energy. International Journal of Hydrogen Energy 23, 661-666.

Landon, J., Demeter, E., İnoğlu, N., Keturakis, C., Wachs, I.E., Vasić, R., Frenkel, A.I., and Kitchin, J.R. (2012). Spectroscopic characterization of mixed Fe–Ni

oxide electrocatalysts for the oxygen evolution reaction in alkaline electrolytes. ACS Catalysis 2, 1793-1801.

Larcher, D., and Tarascon, J.M. (2015). Towards greener and more sustainable batteries for electrical energy storage. Nature Chemistry 7, 19.

Laverdière, J., Jandl, S., Mukhin, A.A., Ivanov, V.Y., Ivanov, V.G., and Iliev, M.N. (2006). Spin-phonon coupling in orthorhombic $RMnO_3$ (R= Pr, Nd, Sm, Eu, Gd, Tb, Dy, Ho, Y): a Raman study. Physical Review B 73, 214301.

Ledinský, M., Fekete, L., Stuchlík, J., Mates, T., Fejfar, A., and Kočka, J. (2006). Characterization of mixed phase silicon by Raman spectroscopy. Journal of Non-Crystalline Solids 352, 1209-1212.

LeRoy, R.L. (1983). Industrial water electrolysis: present and future. International Journal of Hydrogen Energy 8, 401-417.

Lewis, N.S., and Nocera, D.G. (2006). Powering the planet: chemical challenges in solar energy utilization. Proceedings of the National Academy of Sciences of the United States of America 103, 15729-15735.

Li, Y.-F., and Selloni, A. (2014). Mechanism and activity of water oxidation on selected surfaces of pure and Fe-doped NiO_x. ACS Catalysis 4, 1148-1153.

Liu, C., Li, F., Ma, L. P., and Cheng, H. M. (2010). Advanced materials for energy storage. Advanced materials, 22(8), E28-E62.

Lockwood, D.J., and Cottam, M.G. (1988). The spin‐phonon intera ction in FeF_2 and MnF_2 studied by Raman spectroscopy. Journal of Applied Physics 64, 5876-5878.

Long, X., Li, J., Xiao, S., Yan, K., Wang, Z., Chen, H., and Yang, S. (2014). A strongly coupled graphene and FeNi double hydroxide hybrid as an excellent electrocatalyst for the oxygen evolution reaction. Angewandte Chemie International Edition 53, 7584-7588.

Lu, Z., Xu, W., Zhu, W., Yang, Q., Lei, X., Liu, J., Li, Y., Sun, X., and Duan, X. (2014). Three-dimensional NiFe layered double hydroxide film for high-efficiency oxygen evolution reaction. Chemical Communications 50, 6479-6482.

Lukowski, M.A., Daniel, A.S., Meng, F., Forticaux, A., Li, L., and Jin, S. (2013). Enhanced hydrogen evolution catalysis from chemically exfoliated metallic MoS_2 nanosheets. Journal of the American Chemical Society 135, 10274-10277.

Mather, R.R. (2009). 13 - Surface modification of textiles by plasma treatments. In Surface Modification of Textiles, Q. Wei, ed. (Woodhead Publishing), pp. 296-317.

Matsumoto, Y., and Sato, E. (1986). Electrocatalytic properties of transition metal oxides for oxygen evolution reaction. Materials Chemistry and Physics 14, 397-426.

Mazumder, N., Sen, D., Ghorai, U.K., Roy, R., Saha, S., Das, N.S., and Chattopadhyay, K.K. (2013). Realizing Direct Gap, Polytype, Group IIIA Delafossite: Ab Initio Forecast and Experimental Validation Considering Prototype $CuAlO_2$. The Journal of Physical Chemistry Letters 4, 3539-3543.

McCrory, C.C.L., Jung, S., Ferrer, I.M., Chatman, S.M., Peters, J.C., and Jaramillo, T.F. (2015). Benchmarking Hydrogen Evolving Reaction and Oxygen Evolving Reaction Electrocatalysts for Solar Water Splitting Devices. Journal of the American Chemical Society 137, 4347-4357.

McCrory, C.C.L., Jung, S., Peters, J.C., and Jaramillo, T.F. (2013). Benchmarking heterogeneous electrocatalysts for the oxygen evolution reaction. Journal of the American Chemical Society 135, 16977-16987.

Meyer, B.K., Polity, A., Reppin, D., Becker, M., Hering, P., Klar, P.J., Sander, T., Reindl, C., Benz, J., Eickhoff, M., et al. (2012). Binary copper oxide semiconductors: From materials towards devices. physica status solidi (b) 249, 1487-1509.

Mondal, M., Khanra, S., Tiwari, O.N., Gayen, K., and Halder, G.N. (2016). Role of carbonic anhydrase on the way to biological carbon capture through microalgae—A mini review. Environmental Progress & Sustainable Energy 35, 1605-1615.

Nair, P.K., Nair, M.T.S., García, V.M., Arenas, O.L., Peña, A.C.Y., Ayala, I.T., Gomezdaza, O., Sánchez, A., Campos, J., Hu, H., et al. (1998). Semiconductor thin films by chemical bath deposition for solar energy related applications. Solar Energy Materials and Solar Cells 52, 313-344.

Napp, T.A., Gambhir, A., Hills, T.P., Florin, N., and Fennell, P.S. (2014). A review of the technologies, economics and policy instruments for decarbonising energy-intensive manufacturing industries. Renewable and Sustainable Energy Reviews 30, 616-640.

Naylor, C.C., Meier, R.J., Kip, B.J., Williams, K.P.J., Mason, S.M., Conroy, N., and Gerrard, D.L. (1995). Raman spectroscopy employed for the determination of the intermediate phase in polyethylene. Macromolecules 28, 2969-2978.

Nicol, J.M. (1992). Chemisorbed hydrogen and hydrogenous molecules. Spectrochimica Acta Part A: Molecular Spectroscopy 48, 313-327.

Nocera, D.G. (2006). On the future of global energy. Daedalus 135, 112-115.

Nocera, D.G. (2017). Solar Fuels and solar chemicals industry. Accounts of Chemical Research 50, 616-619.

Nørskov, J.K., Bligaard, T., Logadottir, A., Kitchin, J., Chen, J.G., Pandelov, S., and Stimming, U. (2005). Trends in the exchange current for hydrogen evolution. Journal of the Electrochemical Society 152, J23-J26.

Osada, M., Kakihana, M., Wada, S., Noma, T., and Cho, W.-S. (1999). Broken symmetry in low-temperature $BaTiO_3$ phases: Strain effects probed by Raman scattering. Applied Physics Letters 75, 3393-3395.

Osterloh, F.E. (2013). Inorganic nanostructures for photoelectrochemical and photocatalytic water splitting. Chemical Society Reviews 42, 2294-2320.

Paracchino, A., Brauer, J.C., Moser, J.-E., Thimsen, E., and Graetzel, M. (2012). Synthesis and characterization of high-photoactivity electrodeposited Cu_2O solar absorber by photoelectrochemistry and ultrafast spectroscopy. The Journal of Physical Chemistry C 116, 7341-7350.

Parsons, R. (1958). The rate of electrolytic hydrogen evolution and the heat of adsorption of hydrogen. Transactions of the Faraday Society 54, 1053-1063.

Pebley, A.C., Decolvenaere, E., Pollock, T.M., and Gordon, M.J. (2017). Oxygen evolution on Fe-doped NiO electrocatalysts deposited via microplasma. Nanoscale 9, 15070-15082.

Pellicer-Porres, J., Martínez-García, D., Segura, A., Rodríguez-Hernández, P., Muñoz, A., Chervin, J.C., Garro, N., and Kim, D. (2006). Pressure and temperature dependence of the lattice dynamics of $CuAlO_2$ investigated by Raman scattering experiments and ab initio calculations. Physical Review B 74, 184301.

Pilavachi, P.A., Chatzipanagi, A.I., and Spyropoulou, A.I. (2009). Evaluation of hydrogen production methods using the Analytic Hierarchy Process. International Journal of Hydrogen Energy 34, 5294-5303.

Pletcher, D., and Li, X. (2011). Prospects for alkaline zero gap water electrolysers for hydrogen production. International Journal of Hydrogen Energy 36, 15089-15104.

Qiu, Z., Huang, H., Du, J., Tao, X., Xia, Y., Feng, T., Gan, Y., and Zhang, W. (2014). Biotemplated synthesis of bark-structured TiC nanowires as Pt catalyst supports with enhanced electrocatalytic activity and durability for methanol oxidation. Journal of Materials Chemistry A 2, 8003-8008.

Qiu, Z., Ma, Y., Edström, K., Niklasson, G.A., and Edvinsson, T. (2017). Controlled crystal growth orientation and surface charge effects in self-assembled nickel oxide nanoflakes and their activity for the oxygen evolution reaction. International Journal of Hydrogen Energy 42, 28397-28407.

Randles, J.E.B. (1947). Kinetics of rapid electrode reactions. Discussions of the Faraday Society 1, 11-19.

Rao, B.G., Mukherjee, D., and Reddy, B.M. (2017). Chapter 1 - Novel approaches for preparation of nanoparticles. In Nanostructures for Novel Therapy, D. Ficai, and A.M. Grumezescu, eds. (Elsevier), pp. 1-36.

Rashid, M.M., Al Mesfer, M.K., Naseem, H., and Danish, M. (2015). Hydrogen production by water electrolysis: a review of alkaline water electrolysis, PEM water electrolysis and high temperature water electrolysis. International Journal of Engineering and Advanced Technology 4, 2249-8958.

Reier, T., Nong, H.N., Teschner, D., Schlögl, R., and Strasser, P. (2017). Electrocatalytic oxygen evolution reaction in acidic environments – reaction mechanisms and catalysts. Advanced Energy Materials 7, 1601275.

Santos, D.M., Sequeira, C.A., and Figueiredo, J.L. (2013). Hydrogen production by alkaline water electrolysis. Química Nova 36, 1176-1193.

Schalenbach, M., Tjarks, G., Carmo, M., Lueke, W., Mueller, M., and Stolten, D. (2016). Acidic or alkaline? Towards a new perspective on the efficiency of water electrolysis. Journal of The Electrochemical Society 163, F3197-F3208.

Seh, Z.W., Kibsgaard, J., Dickens, C.F., Chorkendorff, I., Nørskov, J.K., and Jaramillo, T.F. (2017). Combining theory and experiment in electrocatalysis: Insights into materials design. Science (New York, NY) 355, eaad4998.

Shi, Y., and Zhang, B. (2016). Recent advances in transition metal phosphide nanomaterials: synthesis and applications in hydrogen evolution reaction. Chemical Society Reviews 45, 1529-1541.

Shinagawa, T., Garcia-Esparza, A.T., and Takanabe, K. (2015). Insight on Tafel slopes from a microkinetic analysis of aqueous electrocatalysis for energy conversion. Scientific Reports 5, 13801.

Socrates, G. (2004). Infrared and Raman characteristic group frequencies: tables and charts (John Wiley & Sons).

Stamenkovic, V.R., Strmcnik, D., Lopes, P.P., and Markovic, N.M. (2017). Energy and fuels from electrochemical interfaces. Nature Materials 16, 57.

Stockmeyer, R., Stortnik, H., Natkaniec, I., and Mayer, J. (1980). Dynamics of hydrogen and water adsorbed on nickel catalysts. Berichte der Bunsengesellschaft für physikalische Chemie 84, 79-84.

Strobl, G.R., and Hagedorn, W. (1978). Raman spectroscopic method for determining the crystallinity of polyethylene. Journal of Polymer Science: Polymer Physics Edition 16, 1181-1193.

Subbaraman, R., Tripkovic, D., Chang, K.-C., Strmcnik, D., Paulikas, A.P., Hirunsit, P., Chan, M., Greeley, J., Stamenkovic, V., and Markovic, N.M. (2012). Trends in activity for the water electrolyser reactions on 3d M(Ni,Co,Fe,Mn) hydr(oxy)oxide catalysts. Nature Materials 11, 550.

Suen, N.-T., Hung, S.-F., Quan, Q., Zhang, N., Xu, Y.-J., and Chen, H.M. (2017). Electrocatalysis for the oxygen evolution reaction: recent development and future perspectives. Chemical Society Reviews 46, 337-365.

Thompson, C., and Cheng, W.P. (2011). Chapter 7—Chemically modified polyelectrolytes for intestinal peptide and protein delivery. In peptide and protein delivery, C. Van Der Walle, ed. (Boston: Academic Press), pp. 123-164.

Tollefson, J. (2010). Hydrogen vehicles: fuel of the future? Nature News 464, 1262-1264.

Torelli, D.A., Francis, S.A., Crompton, J.C., Javier, A., Thompson, J.R., Brunschwig, B.S., Soriaga, M.P., and Lewis, N.S. (2016). Nickel–gallium-catalyzed electrochemical reduction of CO_2 to highly reduced products at low overpotentials. ACS Catalysis 6, 2100-2104.

Trasatti, S. (1972). Work function, electronegativity, and electrochemical behaviour of metals: III. Electrolytic hydrogen evolution in acid solutions. Journal of Electroanalytical Chemistry and Interfacial Electrochemistry 39, 163-184.

Turner, J.A. (1999). A realizable renewable energy future. Science (New York, NY) 285, 687-689.

Turner, J.A. (2004). Sustainable hydrogen production. Science (New York, NY) 305, 972-974.

Vasileff, A., Zheng, Y., and Qiao, S.Z. (2017). Carbon solving carbon's problems: recent progress of nanostructured carbon-based catalysts for the electrochemical reduction of CO_2. Advanced Energy Materials 7, 1700759.

Van Troostwijk, A. P., and Deiman, J. R. (1789). Sur une maniere de décomposer l'eau en air inflammable et en air vital. Obs Phys, 35, 369-378.

Vij, V., Sultan, S., Harzandi, A.M., Meena, A., Tiwari, J.N., Lee, W.-G., Yoon, T., and Kim, K.S. (2017). Nickel-based electrocatalysts for energy-related applications: oxygen reduction, oxygen evolution, and hydrogen evolution reactions. ACS Catalysis 7, 7196-7225.

Wang, J., Xu, F., Jin, H., Chen, Y., and Wang, Y. (2017). Non-noble metal-based carbon composites in hydrogen evolution reaction: fundamentals to applications. Advanced Materials 29, 1605838.

Wang, W. H., Himeda, Y., Muckerman, J. T., Manbeck, G. F., and Fujita, E. (2015). CO_2 hydrogenation to formate and methanol as an alternative to photo-and electrochemical CO_2 reduction. Chemical reviews, 115(23), 12936-12973.

White, R.E., Bockris, J.O., Conway, B.E., and Yeager, E. (1984). Comprehensive treatise of electrochemistry. Vol. 8: experimental methods in electrochemistry (Plenum Press).

Whiteley, K.S., Heggs, T.G., Koch, H., Mawer, R.L., and Immel, W. (2000). Polyolefins. in Ullmann's encyclopedia of industrial chemistry (Wiley), pp. 1-103.

Wu, Z., Zou, Z., Huang, J., and Gao, F. (2018). Fe-doped NiO mesoporous nanosheets array for highly efficient overall water splitting. Journal of Catalysis 358, 243-252.

Xiao, P., Chen, W., and Wang, X. (2015). A Review of phosphide-based materials for electrocatalytic hydrogen evolution. Advanced Energy Materials 5, 1500985.

Yan, Y., Xia, B.Y., Zhao, B., and Wang, X. (2016). A review on noble-metal-free bifunctional heterogeneous catalysts for overall electrochemical water splitting. Journal of Materials Chemistry A 4, 17587-17603.

Yang, H., Irudayaraj, J., and Paradkar, M.M. (2005). Discriminant analysis of edible oils and fats by FTIR, FT-NIR and FT-Raman spectroscopy. Food Chemistry 93, 25-32.

Yeo, B.S., and Bell, A.T. (2012). In-situ Raman study of nickel oxide and gold-supported nickel oxide catalysts for the electrochemical evolution of oxygen. The Journal of Physical Chemistry C 116, 8394-8400.

Yu, J., Low, J., Xiao, W., Zhou, P., and Jaroniec, M. (2014). Enhanced Photocatalytic CO_2-Reduction Activity of Anatase TiO_2 by Coexposed {001} and {101} Facets. Journal of the American Chemical Society 136, 8839-8842.

Zeng, K., and Zhang, D. (2010). Recent progress in alkaline water electrolysis for hydrogen production and applications. Progress in Energy and Combustion Science 36, 307-326.

Zhang, L., Zhao, Z.-J., and Gong, J. (2017). Nanostructured materials for heterogeneous electrocatalytic CO_2 reduction and their related reaction mechanisms. Angewandte Chemie International Edition 56, 11326-11353.

Zhang, W., Hu, Y., Ma, L., Zhu, G., Wang, Y., Xue, X., Chen, R., Yang, S., and Jin, Z. (2018). Progress and perspective of electrocatalytic CO_2 reduction for renewable carbonaceous fuels and chemicals. Advanced Science 5, 1700275.

Zhao, B., Ke, X.-K., Bao, J.-H., Wang, C.-L., Dong, L., Chen, Y.-W., and Chen, H.-L. (2009). Synthesis of flower-like NiO and effects of morphology on its catalytic properties. The Journal of Physical Chemistry C 113, 14440-14447.

Zhu, J., Gui, Z., Ding, Y., Wang, Z., Hu, Y., and Zou, M. (2007). A facile route to oriented nickel hydroxide nanocolumns and porous nickel oxide. The Journal of Physical Chemistry C 111, 5622-5627.

Acta Universitatis Upsaliensis

*Digital Comprehensive Summaries of Uppsala Dissertations
from the Faculty of Science and Technology* 1791

Editor: The Dean of the Faculty of Science and Technology

A doctoral dissertation from the Faculty of Science and
Technology, Uppsala University, is usually a summary of a
number of papers. A few copies of the complete dissertation
are kept at major Swedish research libraries, while the
summary alone is distributed internationally through
the series Digital Comprehensive Summaries of Uppsala
Dissertations from the Faculty of Science and Technology.
(Prior to January, 2005, the series was published under the
title "Comprehensive Summaries of Uppsala Dissertations
from the Faculty of Science and Technology".)